Title: N-dihydrogalactochitosan reduces mortality in a lethal mouse model of SARS-CoV-2

Single Sentence Summary: The immunoadjuvant N-dihydrogalactochitosan diminishes SARS-CoV-2 disease in humanized ACE2 mice, representing a new countermeasure against COVID-19.

Authors: Christopher M. Weiss[1,5], Hongwei Liu[1], Erin E. Ball[1,6], Ashley R. Hoover[2], Talia S. Wong[1], Chun Fung Wong[3], Samuel Lam[3], Tomas Hode[3], M. Kevin Keel[1], Richard M. Levenson[4], Wei R. Chen[2], and Lark L. Coffey[1]*

[1] Department of Pathology, Microbiology & Immunology, University of California, Davis, CA

[2] Stephenson School of Biomedical Engineering, University of Oklahoma, Norman, OK, USA

[3] Immunophotonics, Inc., Saint Louis, MO

[4] Department of Pathology and Laboratory Medicine, UC Davis Health, Sacramento, CA

[5] Current address: MRIGlobal, Kansas City, MO

[6]Current address: Armed Forces Research Institute of Medical Sciences (AFRIMS), Bangkok, Thailand

*Corresponding Author

lcoffey@ucdavis.edu

24 ORCID iD:

25 Christopher Weiss 0000-0003-4704-9533

26 Hongwei Liu 0000-0002-8342-2545

27 Erin Ball 0000-0002-8464-6612

28 Richard Levenson 0000-0002-0112-6823

29 Lark Coffey 0000-0002-0718-5146

30 Wei R. Chen 0000-0002-7133-5794

ABSTRACT

The rapid emergence and global dissemination of SARS-CoV-2 that causes COVID-19 continues to cause an unprecedented global health burden resulting in nearly 7 million deaths. While multiple vaccine countermeasures have been approved for emergency use, additional treatments are still needed due to sluggish vaccine rollout, vaccine hesitancy, and inefficient vaccine-mediated protection. Immunoadjuvant compounds delivered intranasally can guide non-specific innate immune responses during the critical early stages of viral replication, reducing morbidity and mortality. N-dihydro**g**alacto**c**hitosan (GC) is a novel mucoadhesive immunostimulatory polymer of β-0-4-linked N-acetylglucosamine that is solubilized by the conjugation of galactose glycans with current applications as a cancer immunotherapeutic. We tested GC as a potential countermeasure for COVID-19. GC was well-tolerated and did not produce histopathologic lesions in the mouse lung. GC administered intranasally before and after SARS-CoV-2 exposure diminished morbidity and mortality in humanized ACE2 receptor expressing mice by up to 75% and reduced infectious virus levels in the upper airway. Fluorescent labeling of GC shows that it is confined to the lumen or superficial mucosa of the nasal cavity, without involvement of adjacent or deeper tissues. Our findings demonstrate a new application for soluble immunoadjuvants such as GC for preventing disease associated with SARS-CoV-2 and may be particularly attractive to persons who are needle-averse.

IMPORTANCE

The ongoing COVID-19 pandemic necessitates new approaches to reduce disease caused by SARS-CoV-2. We tested the immunoadjuvant N-dihydro**g**alacto**c**hitosan (GC), used previously as an immunostimulant for tumor therapy and adjuvant for viral vaccines, as a potential COVID-19 countermeasure. When GC was administered before and after inoculation of a lethal dose of SARS-CoV-2 into the nose of humanized mice expressing an entry receptor for the virus, fewer mice showed weight loss and died compared to mice that received only the vehicle but no GC. GC-treated mice also had lower levels of infectious SARS-CoV-2 in their upper airway. These results suggest that GC may be a candidate to prevent or treat COVID-19.

INTRODUCTION

Severe acute respiratory syndrome-like coronavirus 2 (SARS-CoV-2) that was first identified from a cluster of viral pneumonia cases in Wuhan, China in December 2019 [1] has caused more than 670 million cases and nearly 6.9 million deaths globally as of March 2023[2]. Clinical manifestations of 2019 novel coronavirus disease (COVID-19) caused by SARS-CoV-2 typically include fever, non-productive cough, and mild to moderate dyspnea, with severe cases developing pneumonia and acute respiratory distress syndrome [1,3,4]. SARS-CoV-2 morbidity and mortality increase with age and systemic proinflammatory and cardiovascular co-morbidities [1,3,5]. Recovered patients may also exhibit long-duration symptoms including disruption to sensations of taste and smell, and cognitive impairment (colloquially referred to as “brain fog”) resulting from neurological involvement [6,7].

Like SARS-CoV, SARS-CoV-2 uses the angiotensin converting enzyme 2 (ACE2) for cell entry [8,9]. Small animals including mice, hamsters, and ferrets, have been fundamental in defining SARS-CoV-2 pathogenesis and developing medical countermeasures [10,11]. Transgenic mice expressing the human ACE2 (hACE2) gene from the human cytokeratin 18 (K18) promoter have served as an especially useful model of severe disease due to well characterized genetics and ease of use [12–14]. Intranasal inoculation of K18-hACE2 mice (hereafter termed hACE2) with SARS-CoV-2 results in a high viral burden in the lungs, which diminishes past day 7, and elevated viral loads detectible in the brain at day 7 [13].

SARS-CoV-2, which can be transmitted in small-droplet aerosols from person to person, can take up to 14 days to produce symptoms [15]. Public health countermeasures have evolved as additional treatments and information regarding transmission risks for COVID-19 have become available. In addition to face coverings and physical distancing, multiple vaccine candidates and therapeutic interventions have now received emergency use authorization by the United States Food and Drug Administration (FDA) [16]. While ‘herd immunity’ through vaccination remains the target, it is estimated that 70-90% of the global population must be immune in order to interrupt transmission [17]. This target becomes even more challenging with high levels of vaccine skepticism, slow production, inequitable distribution, and the rise of variants of concern capable of more efficient transmission or vaccine escape. Pre- and post-exposure countermeasures can help fill the vaccine gap by reducing COVID-19 morbidity and mortality in unprotected communities and thus reduce the global burden of the pandemic. The nucleoside analog, remdesivir [18], is the only current FDA-

98 approved therapeutic approved for non-hospitalized COVID-19 patients and was
99 authorized based on its ability to shorten recovery time [19], but it is not ideal for clinical
100 use due to its only moderate clinical efficacy [20], as well as its requirement for
101 intravenous administration. Although there are many active trials of therapeutic agents
102 with more than 10 drugs or biological products holding emergency use authorization,
103 including Nirmatrelvir/Ritonavir (Paxlovid) and Molnupiravir (Lagevrio), most are
104 indicated for patients with severe COVID-19 [21,22]. Despite these advances, there are
105 presently no drugs available for high-risk exposure use to protect against SARS-CoV-2.
106 To circumvent this gap, we repurposed an immunostimulant used for cancer
107 immunotherapy and as a vaccine adjuvant with a goal of mitigating COVID-19 disease.
108 The parent compound of GC, chitosan, is a linear biological polysaccharide
109 polymer of β-0-4-linked N-acetylglucosamine and is produced from alkaline treatment of
110 the chitin exoskeleton of crustaceans. Chitosan is approved by the FDA for tissue
111 engineering and drug delivery. Chitosan shows broad-acting antiviral [23] and
112 immunoadjuvant properties [24,25] including interferon (IFN) induction [26,27] that is
113 critical for viral control [28–30], and has been evaluated as an antiviral therapy for
114 respiratory viruses [31–33]. Chitosan and various derivatives have been explored as
115 COVID-19 treatments and vaccine adjuvants [34–39]. Modification of chitosan by
116 covalently attaching galactose sugars to the free amino acids on the polysaccharide
117 backbone produces N-dihydro**g**alacto**c**hitosan (GC) [40,41]. GC was initially designed
118 to further improve immune-stimulating functionality of the molecular backbone by adding
119 glycan moieties that can bind to C-type lectin receptors on antigen presenting cells [42]
120 and lead to a downstream immune response while retaining the mucoadhesive

121 properties of the parent molecule [43]. Furthermore, GC has improved solubility at
122 physiological pH ranges compared to its parent molecule, and hence is more suitable as
123 an injectable agent. With these modifications, GC has been developed for use in human
124 interventional immuno-oncology to stimulate systemic anti-tumor immunity [44]. GC
125 recruits granulocytes at the injection site [45] and stimulates activation of dendritic cells
126 and macrophages through upregulation of co-stimulatory molecules CD40, CD86, and
127 MHCII *in vitro* and *in vivo* [46,47] . Macrophages also show increased nitric oxide
128 production and phagocytic abilities in response to GC [46]. Single-cell RNA sequencing
129 indicates enrichment of type I IFN signaling in multiple innate immune cells, including
130 monocytes, M1 macrophages, and neutrophils in tumors following GC administration
131 [48]. Our prior work showed that GC mixed with recombinant SARS-COV-2 spike and
132 nucleocapsid antigen vaccines delivered intranasally protects mice from lethal disease
133 after intranasal SARS-CoV-2 inoculation. In that study, when 0.75% GC was delivered
134 intranasally to control mice, $CD45^+$ and B cell cellularity increased in cervical lymph
135 nodes accompanied by an influx of migrating and resident dendritic cells and $CD4^+$ and
136 $CD8^+$ T cells. These data show that GC induces a local immune response that induces
137 lymphocyte migration and activation in the nasal-associated lymphoid tissue
138 (NALT)[49]. The upregulation of innate immune responses and recruitment of cellular
139 responses to the NALT, which is the SARS-CoV-2 exposure site, suggests that broad-
140 acting non-toxic immunoadjuvants such as GC that can be intranasally may modulate
141 SARS-CoV-2 infection. Intranasal instillation may generate a robust immune protection
142 in the upper respiratory tract and may be more widely accepted than vaccine injections.
143 Furthermore, non-specific immunoadjuvants such as GC could offer a benefit over more

144 narrowly targeted antivirals by providing protection against a potentially broad range of
145 pathogens, potentially including future agents not yet affecting public health.
146 In the present study, we explored the use of GC for prophylaxis against SARS-
147 CoV-2 infection applied pre- and post-exposure to lethal dosages of the virus in
148 transgenic hACE2 mice. To simulate the use of solubilized GC as a nasal spray, we
149 applied the compound intranasally twice before exposure and once following exposure
150 of mice to a human isolate of SARS-CoV-2. Our data demonstrate a strong protective
151 effect of GC in preventing mortality in this lethal model of disease. Fluorescent-labeled
152 GC administered intranasally remained in the nasal cavity. Pre- and post-exposure
153 countermeasures may help fill the vaccine gap by reducing COVID-19 morbidity and
154 mortality and reduce the global burden of the pandemic.
155

156 **RESULTS**

157 **N-dihydrogalactochitosan reduces SARS-CoV-2-associated mortality in hACE2**
158 **transgenic mice.**

159 To determine the antiviral efficacy of N-dihydro**g**alacto**c**hitosan (GC) against SARS-
160 CoV-2, 6-week-old hACE2 [B6.Cg-Tg(K18-ACE2)2Prlmn/J] mice were treated
161 intranasally (i.n.) with 0.75% GC in neutral buffered saline 3 and 1 days prior to virus
162 exposure and then 1 day post exposure (**Fig. 1a**). To ensure that the dose, schedule,
163 and route of GC administration were well tolerated, pilot studies using 14 additional
164 male and female hACE2 mice showed that GC treatment alone does not produce
165 adverse clinical signs or pulmonary lesions. Lung histologic scores in mice administered
166 GC were not significantly different from mice treated with PBS (**Supplementary Fig. 1,**

167 **Supplementary Table 1**). Mice were inoculated i.n. 1 day prior to the final GC
168 treatment with 10^3 or 10^4 plaque forming units (PFU) of SARS-CoV-2, a route and dose
169 intended to produce high lethality in this model. Inocula were back-titrated to verify the
170 administered dose. Tracheal swabs were collected for the first 3 days post inoculation
171 and animals were monitored daily until day 14 for weight loss and health status.
172
173 **Fig. 1: N-dihydrogalactochitosan protects mice from SARS-CoV-2 mortality. (a)**
174 **Experimental design** where 6-week-old male and female hACE2 transgenic mice were
175 treated with 0.75% GC or PBS delivery vehicle at days -3, -1 and +1 post-inoculation.
176 Mice were inoculated at day 0 with 103 or 104 PFU of SARS-CoV-2 or PBS (mock).
177 Animals were weighed daily, and throats were swabbed on days 1 through 3. (**b**)
178 **Weight** represented as a percentage of individual mouse weight at the time of
179 inoculation. A main effect only model two-way ANOVA with Tukey corrected multiple
180 comparisons yielded an F=52.80, p<0.0001, 4 degrees of freedom. Each symbol
181 represents an individual mouse, and the horizontal lines show geometric mean and
182 error bars are geometric standard deviation. **(c) Survival proportions.** The solid lines
183 are survival proportions, and the shaded boxes show 95% confidence intervals. **(d)**
184 **Logrank Mantel-Cox comparisons of survival proportions** with Bonferroni corrected
185 p-values, multiple pairwise tests, 1 degree of freedom. n=8-16 per group, 2 combined
186 experiments.
187
188 Weight remained stable for the first 3 days in all groups. Weight in infected mice
189 that were not GC-treated rapidly declined, starting at day 4 in the 10^4 PFU group, and at

190 day 5 in the 10^3 PFU groups (**Fig. 1b**). Half of the GC-treated mice administered 10^4
191 PFU experienced no weight loss throughout the duration of the study (**Supplementary**
192 **Fig. 2**); conversely, their growth outpaced mock-infected counterparts treated with
193 saline alone ($p<0.0001$). This effect was not limited to one biological sex and did not
194 correlate with mouse starting weight at the time of study initiation. Additional mice lost
195 weight starting at day 4 but did not reach euthanasia criteria (loss of 20% of initial body
196 weight) and recovered to starting weight by day 10 post-inoculation. Relative to the 10^4
197 group, mice inoculated with 10^3 PFU SARS-CoV-2 exhibited delayed or transient weight
198 loss, with 2 mice experiencing no weight loss over the duration of the study. At the
199 higher inoculation dose of 10^4 PFU, GC significantly reduced weight loss versus
200 delivery vehicle treated controls ($p<0.0001$). At the lower 10^3 PFU inoculation dose, GC
201 trended toward protection from weight loss, which was confounded by non-uniform
202 disease in delivery vehicle treated controls ($p=0.11$). Mice treated with delivery vehicle
203 and inoculated with 10^3 or 10^4 PFU had a median survival time of 7±3.3 and 6.5±0.9
204 days, respectively (**Fig. 1c**). At the lower inoculation dose of 10^3 PFU, GC had an
205 efficacy of 37.5% protection from mortality ($p=0.05$) (**Fig. 1c**). At the higher inoculation
206 dose of 10^4 PFU, GC reduced SARS-CoV-2 mortality by 75% ($p<0.0001$) (**Fig. 1d**).
207 Together, these results demonstrate the potent efficacy of GC in preventing fatal SARS-
208 CoV-2 disease in transgenic mice.
209
210 **N-dihydrogalactochitosan reduces SARS-CoV-2 viral levels in the respiratory**
211 **tract.**

212 We next sought to determine whether GC reduced viral levels in addition to protecting
213 mice from mortality. Infectious SARS-CoV-2 levels were assessed longitudinally in mice
214 by swabbing throats from day 1 to 3 post-inoculation (**Fig. 2a**). SARS-CoV-2 was
215 detectible in tracheal swabs of infected animals at day 1 post inoculation and most
216 animals had no detectible virus by day 3. Virus levels were elevated in mice inoculated
217 with 10^4 PFU versus 10^3 PFU at 1 day post inoculation (p=0.05), but differences
218 between inoculation doses were not detected after day 2 (p>0.99). GC significantly
219 reduced virus levels in tracheal swabs at day 1 and day 2 post inoculation with 10^4 PFU
220 (p=0.0005 and p=0.02, respectively). A similar effect was not observed in mice that
221 received the lower inoculum of 10^3 PFU. All delivery vehicle-treated mice had detectible
222 virus in tracheal swabs following infection, while 29.2% (7/24) of GC-treated mice had
223 no infectious virus isolated between days 1 and 3. Positive virus detection in tracheal
224 swabs was not correlated with lethal disease in mice (p=0.62, Fisher's exact test).
225 Cumulative virus levels in tracheal swabs were calculated as area under the curve for
226 individual animals (**Fig. 2b**). GC significantly reduced the total shed virus levels in
227 tracheal swabs in mice inoculated with 10^4 PFU from a geometric mean of 225 to 5.6
228 PFU (p<0.0001) and trended toward a reduction in animals inoculated with 10^3 PFU
229 from 138 to 15 PFU (p=0.08).
230
231 **Fig. 2: N-dihydrogalactochitosan reduces SARS-CoV-2 detection in the**
232 **respiratory tract.** Infectious SARS-CoV-2 was measured in (**a**) **tracheal swabs**
233 collected from hACE2 transgenic mice on days 1, 2 and 3 post inoculation. Repeated
234 measures two-way ANOVA with Tukey corrected multiple comparisons on log10-

transformed values, F=16.96, p<0.0001, 4 degrees of freedom. (**b) Total area under the curve** shows cumulative virus levels in swabs. ANOVA of log10-transformed total peak area with Tukey corrected multiple comparisons, F=7.538, p<0.0001, 4 degrees of freedom. Mice were necropsied on days 6, 7 and 14 post-inoculation as euthanasia criteria were met. Infectious virus levels were measured in (**c**) **lung** and (**d**) **brain** at experimental endpoints. Main effects only model two-way ANOVA on log10-transformed values, F=2.431, p=0.0606, 4 degrees of freedom for lung, F=0.8134, p=0.5229, 4 degrees of freedom for brain. Symbols are individual animals, horizontal lines show geometric mean, and error bars represent geometric standard deviation. n=8-16 per group, 2 combined experiments. LD = limit of detection, AUC = area under the curve. * $p < 0.05$, *** $p < 0.001$, **** $p < 0.0001$.

As individual animals met humane experimental endpoints, mice were euthanized. Infectious virus levels were measured in the lungs (**Fig. 2c**) and brain (**Fig. 2d**) from mice on days 6, 7, and 14. Although mean virus levels were not significantly different, GC treatment trended toward reducing lung virus levels (F=2.431, p=0.06, two-way ANOVA) with cumulative effects in animals inoculated with 10^3 PFU driving the main treatment effect (p=0.06).

Comparatively high viral titers were observed in the brain at the time of death, consistent with previous descriptions in this model [13]. Virus was detectible in the brain in all but 2 infected animals at the time of death, indicating neuroinvasion as a likely cause of morbidity. No significant differences in brain virus levels were observed between treatments (F=0.8134, p=0.52, two-way ANOVA). No infectious virus was detectible in the lungs or brains of animals euthanized at day 14 post inoculation.

258

259 **N-dihydrogalactochitosan reduces the severity of histopathologic lesions**
260 **associated with SARS-CoV-2 infection in lungs.**

261 Intranasal inoculation of hACE2 transgenic mice with PBS followed by mock inoculation
262 resulted in normal lung architecture in most mice, although several animals exhibited
263 mild alveolar septal inflammation, likely associated with i.n. administration **(Fig. 3a)**. By
264 contrast, mice inoculated with 10^3 or 10^4 PFU SARS-CoV-2 (**Fig. 3c**, representative 10^3
265 image shown) exhibited extensive lymphohistiocytic interstitial pneumonia with a
266 peribronchiolar and perivascular distribution and scattered multinucleated syncytial cells
267 7 days post inoculation. Bronchiolitis, bronchiolar epithelial and alveolar septal necrosis,
268 hemorrhage, fibrin, edema, and vascular endothelial inflammation were also
269 occasionally noted. SARS-CoV-2-infected mice treated with GC showed lesser
270 histopathologic lesions in the lung (**Fig. 3b,** representative 10^3 image shown) compared
271 to animals that did not receive GC, and inflammation was focally distributed instead of
272 widespread. To quantify histopathologic changes, lung lesion severity was scored using
273 specific criteria (**Supplementary Table 2**). The percent of the lung that was affected in
274 mice euthanized at 6, 7, or 14 days post inoculation as assessed by image analysis
275 software did not differ significantly between SARS-CoV-2 infected mice treated with GC
276 versus those who were not GC treated(**Fig. 3d**). Despite this, GC treatment significantly
277 reduced the mean lung histopathology severity score across all euthanasia days
278 (although not when the results at days 6 and 7 or 14 were analyzed separately [**Fig.**
279 **3e**]) for mice dosed with 10^4 PFU SARS-CoV-2; scores were reduced from 4.6 to 2.5
280 (ANOVA, $p < 0.0001$) (**Fig. 3f**). Mean scores for mice treated with GC and 10^3 PFU of

281 SARS-CoV-2 trended towards being lower than for mice who did not receive GC but
282 were not significantly different ($p > 0.05$). Together, these data show that GC reduces
283 SARS-CoV-2-induced disease in the lung of hACE2 mice, although only significantly in
284 mice administered the higher 10^4 PFU dose of SARS-CoV-2.
285
286 **Fig. 3: N-dihydrogalactochitosan reduces histopathology associated with SARS-**
287 **CoV-2 infection in lungs.** Lungs from hACE2 transgenic mice were collected at the
288 time of death, thin sectioned, and hematoxylin and eosin stained for histopathological
289 scoring. Images show representative lungs. **(a)** Normal lung from a **PBS-treated, mock**
290 **inoculated mouse at day 14**. Bronchioles lined by epithelial cells, alveolar septa
291 containing pulmonary capillaries lined by pneumocytes, and a small arteriole are visible
292 (inset). **(b)** Lung from a **GC + 10^3 PFU SARS-CoV-2 mouse at day 7** with patchy
293 inflammation (black arrows) distributed around airways and affecting approximately 15%
294 of the section. Peribronchiolar alveolar septal inflammation composed primarily of
295 lymphocytes and macrophages (asterisk, inset) with scattered multinucleated cells. **(c)**
296 Lung from a **PBS + 10^3 PFU SARS-CoV-2 inoculated mouse at day 7** showing
297 widespread, multifocal to coalescing inflammation affecting all lung lobes and
298 approximately 60% of the section. The inset shows lymphohistiocytic bronchoalveolar
299 inflammation (asterisk) with multinucleated syncytial cells (circled), endotheliitis (black
300 arrowheads) and bronchiolar epithelial hyperplasia characterized by disorganization and
301 piling-up of bronchiolar epithelium with increased mitotic figures (black arrows). (**d**)
302 **Total affected lung area** was estimated using image analysis software. **(e-f) Lung**
303 **lesion severity** was scored according to criteria defined in Supplementary Table 1.

304 Scale bars are 2 mm (subgross) and 50 μm (insets). As=alveolar septa, B=bronchioles,
305 Br=bronchus, BV=blood vessel. ** $p < 0.01$, *** $p < 0.001$, **** $p < 0.0001$, ns=not
306 significant. ANOVA, F=35.86, p<0.0001, 4 degrees of freedom (e). ANOVA, F=10.32,
307 p<0.0001, 4 degrees of freedom (e). Symbols are individual animals, bars show the
308 mean, and error bars show the standard deviation, n=8-16 per group, 2 combined
309 experiments.
310
311 **Mice treated with N-dihydrogalactochitosan produce neutralizing antibodies after**
312 **SARS-CoV-2 exposure.**
313 We next sought to determine whether mice surviving SARS-CoV-2 inoculation
314 produced a humoral immune response that might protect them from future infection.
315 Serum from blood collected at day 14 post inoculation was assessed for neutralizing
316 antibody against the inoculation strain of SARS-CoV-2 by plaque reduction
317 neutralization test (PRNT) at the 80% neutralization threshold (**Fig. 4**). All mice
318 surviving virus inoculation generated neutralizing antibodies. Mice in the GC group
319 inoculated with 10^3 or 10^4 PFU generated neutralizing titers of 1:676 and 1:861
320 (geometric mean), respectively. In comparison, PBS-administered mice that received an
321 inoculation dose of 10^3 PFU had a mean neutralizing titer of 1:1448. Neutralizing
322 antibody titers were not different across treatments (p>0.99) or virus dose, although
323 PBS-administered mice inoculated with 10^4 PFU SARS-CoV-2 were unavailable for
324 comparison due to uniform lethality. These data confirm that surviving mice were
325 infected and indicate that animals were able to develop adaptive immune responses
326 that could potentially protect against reinfection.

327

328 **Fig. 4: N-dihydrogalactochitosan treated mice surviving SARS-CoV-2 inoculation**
329 **produce neutralizing antibodies.** Neutralizing antibody was assessed by 80% plaque
330 reduction neutralization test (PRNT80) in serum from hACE2 transgenic mice surviving
331 to day 14 post inoculation. No PBS treated mice inoculated with 104 PFU SARS-CoV-2
332 were available for comparison due to uniform mortality. * $p < 0.05$, ** $p < 0.01$, LD = limit
333 of detection. Kruskal-Wallis test with Dunn corrected multiple comparisons, H=17.87,
334 p=0.0005, 3 degrees of freedom. Symbols are individual animals, horizontal lines are
335 geometric mean and error bars show geometric standard deviation, n=2-12 per group,
336 two combined experiments.

337

338 **Fluorescent labeled N-dihydrogalactochitosan administered intranasally in mice**
339 **localizes to the mucous of the nasal cavity**

340 Finally, we administered fluorescent labeled GC (FITC-GC) i.n. to mice to examine
341 retention kinetics in the nasal concha. Two mice per time point were FITC-GC treated
342 once and then euthanized 2h, 9h, or 2d later, or were treated twice (2X) and harvested
343 3d later; for these mice, the second treatment was administered 1 day before
344 euthanasia. Negative control mice were not administered FITC-GC. Histopathology was
345 evaluated and quantified using a scoring rubric developed for the nasal cavity
346 (**Supplemental Table 3**). Fluorescence in the nasal cavity was visualized with
347 microscopy measured by calculating the percent area of the total nasal conchae per
348 slide with a fluorescent signal. Fluorescing aggregates identified within the oral cavity of
349 several treated mice were not included in the measurements, as they were outside the

350 nasal conchae. Negative control mice had no fluorescent foci (**Fig. 5a**). For FITC-GC
351 treated mice, fluorescing foci were predominantly within the lumen or loosely adhered to
352 the nasal mucosa, with infrequent fluorescing areas within the epithelium (**Fig. 5b-f**).
353 Although small group sizes preclude statistical assessments, the fluorescent signal of
354 FITC-GC in the nasal cavity of all but 1 FITC-GC treated mouse appeared higher than
355 in negative control mice (**Fig. 5g**). Histologically, fluorescent material was typically
356 associated with inflammatory cells, mucous, and debris. Histology scoring in the nasal
357 concha of these mice showed that while PBS treated mice had low scores, FITC-GC
358 treatment increased scores (**Fig. 5h**). Treatment of the group of mice euthanized 3d
359 post treatment with 2 administrations of FITC-GC did not increase the percent nasal
360 concha fluorescent or histology scores. All FITC-GC treated mice showed moderate
361 rhinitis characterized by mixed inflammatory mucosal or submucosal infiltration and or
362 nasal cavity exudate composed of neutrophils, macrophages and lymphocytes and mild
363 to moderate hemorrhage, fibrin, edema, and sometimes necrotic debris. Together,
364 these data support a process whereby GC administered i.n. in mice remains confined to
365 the superficial mucosa and acts as a mild irritant without eliciting deeper inflammation.
366

367 **Fig. 5. Fluorescent labeled GC (FITC-GC) administered intranasally to mice**
368 **localizes to the nasal cavity and immune cell influx results in nasal concha**
369 **histopathology scores.** Fluorescent images of nasal concha from mice administered
370 **(a)** no FITC-GC or (**b-f**) 0.75% FITC-GC i.n. administered once, and euthanized 2h, 9h,
371 2d or 3d later. Mice in the group euthanized 3d after the first treatment were
372 administered a second treatment 1d before euthanasia. Panel (**c**) is at a magnification

373 of 20, (**b-f**) are at a magnification of 20X. NC is nasal conchae, T is tooth, CT is
374 connective tissue. (**g**) Fluorescence measured as percent of total image area, limited to
375 nasal mucosa. Matching symbols for each time show 2 measurements from the same
376 mouse. (**h**) Nasal concha histopathology scores based on the scoring rubric in
377 Supplemental Table 2. N=2 mice per time. The small group size precluded statistical
378 assessments.
379

380 **DISCUSSION**

381 Intranasal administration of GC to prevent or treat SARS-CoV-2 represents a
382 novel application of this potent immunostimulatory compound. In the present study, GC
383 was well-tolerated and prevented lethal disease in up to 75% of treated humanized
384 mice, while all mice not receiving GC but inoculated with 10^4 PFU SARS-CoV-2 required
385 euthanasia. All surviving animals had neutralizing antibodies detectable at 14 days post
386 inoculation. Similar SARS-CoV-2 antibody titers were detected in GC-treated and
387 untreated animals. Mice that received GC treatment also displayed lower levels of
388 infectious SARS-CoV-2 in tracheal swabs collected 1 to 2 days post inoculation.
389 Reducing virus levels in the upper airway has gained particular significance as recent
390 vaccine breakthrough cases with variants of concern demonstrate SARS-CoV-2
391 shedding at similar levels to unvaccinated individuals, which is a key determinant of
392 transmission potential [50]. Our findings demonstrate a reduction in viral burden and
393 virus-induced disease along with a resultant increase in survival due to GC treatment.
394 GC is a polymeric mixture containing strands of varying lengths of selectively
395 galactose-conjugated and partially deacetylated β-0-4-linked N-acetylglucosamine

396 molecules with a specific range of molecular weights [40,41,44,45]. Synthesized and
397 purified under Good Manufacturing Practice (GMP) conditions, N-
398 dihydrogalactochitosan is a well-characterized variant of GC. Characterization and
399 quality control testing ruled out contamination from endotoxins, heavy metals, and other
400 impurities, which eliminates a major confounding factor in the research of these
401 naturally derived molecules, and of chitosan in particular [51]. Water solubility,
402 immunological properties, biocompatibility, and a favorable toxicity profile are key
403 features of GC. The unconjugated base polymer, chitin, is a primary structural
404 component of cell walls for organisms ranging from fungi to arthropods [23]. Chitosan, a
405 derivative of chitin, is deacetylated through alkaline treatment and is marketed as a
406 nutritional supplement [52] and used as a biopolymer [53]. Unmodified chitosan has
407 been used successfully to treat influenza A virus infection in mice [31], demonstrating a
408 potential application as a non-specific antiviral compound for respiratory virus infection.
409 However, unmodified chitosan has low solubility in neutral buffered aqueous solution
410 and requires acidic formulation; poor characterization, purification and lack of controlled
411 synthetic pathways lead to poor reproducibility and unpredictable outcomes [51]. GC
412 circumvents these limitations through a controlled and reproducible process of
413 synthetically attaching galactose to the free-amino groups of the chitosan base,
414 improving solubility (and thus bioavailability) while maintaining a physiological pH. GC
415 has been previously used as a combination anti-tumor therapy due to its
416 immunoadjuvant properties [46,48], but its utility as a broad-acting antiviral compound
417 has not previously been investigated.

418 Immunoadjuvants stimulate non-specific innate immune responses through
419 various mechanisms. Some use pattern-recognition receptors, including the Toll-like
420 receptor (TLR) family of antigen detection complexes. While the mechanism of SARS-
421 CoV-2 protection has not been determined for GC, chitosan, and similar polymers of N-
422 acetylglucosamine, interact with TLR2, which serves as a rationale for inclusion of
423 chitosan as a vaccine adjuvant. TLR2 signals through myeloid differentiation factor 88
424 (MyD88) to stimulate the nuclear factor kappa B (NF-κB) pathway and downstream
425 inflammatory and anti-microbial cytokine responses [54,55]. TLR engagement of the
426 canonical NF-κB pathway up-regulates both tumor necrosis factor alpha (TNF-α) and
427 interleukin-6 (IL-6), two potent pro-inflammatory effectors. IL-6, which is necessary for
428 antiviral immunity against other virus families, has been identified as a target of
429 dysregulation associated with hyperinflammatory responses in the lungs during SARS-
430 family coronavirus infections. SARS-CoV-1 nucleocapsid protein can stimulate NF-κB
431 activation and IL-6 production independent of infection [56]. Prolonged high levels of IL-
432 6 are correlated with severe COVID-19 outcomes in humans, and a similar association
433 has been found in ferrets infected with SARS-CoV-2 [57]. The timing of IL-6 production
434 may play a critical role in determining whether viral clearance is achieved or
435 alternatively, hyperinflammatory responses result. Early, but not late, induction of IL-6
436 during respiratory syncytial virus (RSV), influenza A, and rhinovirus infection promote
437 viral clearance and limit prolonged inflammation by establishing regulatory T cell
438 populations that limit virus spread [58]. Similarly, timed induction of pro-inflammatory
439 responses by GC treatment pre- and post-infection may promote viral clearance before
440 virus-mediated dysregulation of this pathway can occur. As such, future studies should

441 explore the timing of GC treatment and regulation of IL-6 and associated pro-
442 inflammatory pathways.
443 The data in this study demonstrate that treatment with GC does not impact
444 development of a neutralizing antibody response by day 14 after SARS-CoV-2
445 inoculation, even though it reduced infectious SARS-CoV-2 in tracheal swabs. These
446 data suggest GC functions as an immunoadjuvant that can modulate innate immune
447 responses after SARS-CoV-2 infection, leading to stimulation of robust antiviral adaptive
448 immunity. Experimental evidence from cell culture and animal models supports at least
449 four mechanisms by which complex carbohydrates such as GC could stimulate the
450 innate and adaptive immune systems [59–62]. First, GC recognition by sensors on
451 macrophages and dendritic cells (DC) can stimulate innate immune defenses [63–65].
452 While immune receptors for GC have not been identified, chitosan binding to C-type
453 lectin receptors such as dectin-1 can initiate innate immune signaling [66,67]. Second,
454 GC-mediated antigen uptake [68] and antigen presentation by DCs could lead to CD4
455 and CD8 T cell responses [45,46]. Studies in mice show GC induces type 1 IFN [48],
456 leading to enhanced DC activation and robust CD4 T helper cells [60]. Activation of the
457 STING pathway by type I IFN is a known important antiviral pathway independent of
458 neutralizing antibodies[49]. Notably, DNA sensor activation is mediated by chitosan-
459 induced cellular DNA release. Third, physical antigen sequestration and slow antigen
460 release within draining lymph nodes facilitated by GC could potentially prolong germinal
461 center reactions, thereby enhancing humoral immunity by fostering affinity maturation of
462 B cells [69,70]. Fourth, GC triggers recruitment of neutrophils, macrophages, and
463 lymphocytes in the nasal cavity indicating a heightened innate immune response that

464 could eliminate SARS-CoV-2 (and other respiratory pathogens) and infected cells at the
465 entry site via mechanisms such as phagocytosis, formation of neutrophil extracellular
466 traps, the release of reactive oxygen species, and inflammatory cytokines such as IL-
467 1β, TNFα, that recruits more leukocytes. Thus, GC may have potential as a dual-
468 purpose preventative and therapeutic with immunostimulatory properties. Future studies
469 are needed to investigate the impact of GC on SARS-CoV-2-specific immune
470 responses.

471 In addition to the immunoadjuvant properties of GC, direct interactions between
472 GC and SARS-CoV-2 in the nasal cavity may contribute to the protection we observed
473 in mice. As the nasopharyngeal and oral cavity are often the primary entry sites of
474 SARS-CoV-2 and other respiratory viruses, interventions or medications at these
475 locations could provide an important boost in the first line of defense. The reduction in
476 SARS-CoV-2 levels in GC treated mice in the first 2 days post-inoculation suggests that
477 GC has early effects that hamper the initial phase of viral infection, especially given that
478 serum neutralizing antibodies are not detectable before about 7 days. Although we
479 observed that GC reduced tracheal swab titers, we acknowledge that tracheal swabs
480 may less accurately represent virus levels in the upper respiratory tract compared to
481 nasal turbinates. Additionally, GC is viscous, and its cationic charge allows it to bind to
482 negatively charged biomolecules (such as mucin) and act as a mucoadhesive. Our
483 labeling studies with FITC-GC show it remains in the nasal cavity after intranasal
484 administration. GC present at the time of infection may therefore act as a physical
485 barrier and/or directly inactivate SARS-CoV-2 before it can initiate infection. Additional
486 studies of the temporal kinetics of GC bioavailability and detailed studies of GC-virus

interactions to establish whether GC blocks virus entry and/or replication are needed to establish mechanisms of protection; these experiments could also clarify why greater protection from lethal disease was observed after inoculation with the higher SARS-CoV-2 dose in these studies.

In summary, we show here that GC treatment of humanized mice pre- and post-infection with SARS-CoV-2 reduces lethal disease, virus levels in the upper respiratory tract, and significant lesions in the lungs. These data suggest a possible role of GC as a SARS-CoV-2 countermeasure. Additional pre-clinical studies could focus on the mechanism of protection, including further assessment of the antiviral and immunomodulatory effects of GC. Future studies should also determine optimal GC dose and schedule that would confer the greatest benefit in reducing disease, as well as to determine whether GC confers both prophylactic and therapeutic benefits in mice that are euthanized at pre-determined intervals instead of when they meet euthanasia criteria.

METHODS

Ethics Statement: Mouse work was conducted on protocols #21868 (University of California, Davis), # R20-026 (University of Oklahoma) and # AUP007 (Immunophotonics). Each institutional animal care and use committee (IACUC) approved all mouse work. Infectious virus was handled in certified animal biosafety level 3 laboratory (ABSL-3) spaces in compliance with approved institutional biological use authorization #R2813. The University of California, Davis, is accredited by the

510 Association for Assessment and Accreditation of Laboratory Animal Care (AAALAC). All
511 mouse work adhered to the NIH Guide for the Care and Use of Laboratory Animals[71].
512 ***Mice:*** Equal numbers of male and female transgenic mice expressing the human ACE2
513 receptor on a K18 transgene in a C57Bl/6J background (B6.Cg-Tg(K18-ACE2)2Prlmn/J,
514 referenced as 'hACE2') were purchased at 5 weeks of age from Jackson Laboratories
515 (Sacramento, CA) and acclimated for up to 6 days. C57BL/6 mice treated with
516 fluorescent GC were used at 6-8 weeks of age and were purchased from Jackson
517 Laboratories. Mice for SARS-CoV-2 studies were co-housed by sex in ABSL-3
518 conditions. At all 3 institutions, mice were housed in groups of up to 4 animals per cage
519 at 22-25°C and a 12:12 hour light: dark cycle. Rodent chow with 18% protein content
520 and sterile bottled water was provided *ad libitum* for the duration of the experiment.
521 ***Virus:*** SARS-CoV-2/human/USA/CA-CZB-59X002/2020 (GenBank #MT394528), which
522 was isolated from a patient in 2020 in Northern California and passaged once in Vero-
523 E6 cells, was generously provided by Dr. Christopher Miller (University of California,
524 Davis). To generate stocks for these studies, SARS-CoV-2 was passaged one
525 additional time in Vero-E6 cells to achieve a titer of 2.2 x 107 plaque forming units
526 (PFU)/mL. Single-use virus aliquots were stored at -80°C.
527 ***N-dihydrogalactochitosan Treatment*****:** Sterile 1% weight/volume N-
528 dihydrogalactochitosan (GC) was provided by Immunophotonics. GC was generated
529 using Good Manufacturing Practices (GMP). Testing of GC included appearance,
530 identity (1H NMR and UV/Vis), assay (HPLC), degree of galactation (1H NMR),
531 viscosity, specific gravity, pH, microbiological (endotoxins and sterility), subvisible
532 particulate matter, impurities (boron, galactose, galactitol, transition metals), molecular

533 weight, and polydispersity indices. GC was presented as a 1.0% sterile solution (10
534 mg/ml) in 5 ml sealed vials and was diluted with sterile deionized water and sterile
535 filtered 20X phosphate buffered saline (PBS) to a final concentration of 0.75% GC and
536 1X PBS. Mice were anesthetized with isoflurane and 40 µL of either diluted GC or PBS
537 delivery vehicle was administered intranasally (i.n.) by a hanging drop over both nares.
538 Mice were treated identically at 3 days and 1 day prior to inoculation and 1 day post
539 inoculation. Six-week-old male (N=7) and female (N=7) mice were used to assess the
540 histopathologic effects of GC on the murine lung. Mice were GC treated on the same
541 schedule as above, and a subset were euthanized 2 or 14 days after the last GC
542 treatment. Cumulative lung lesion scores were determined using a scoring scale
543 (**Supplementary Table 2**).
544 ***SARS-CoV-2 Inoculation***: At inoculation, mice were anesthetized and administered 30
545 µL of PBS or SARS-CoV-2 diluted in PBS at a dose of 103 or 104 PFU i.n. via hanging
546 drop. Inocula were back-titrated to confirm the target dose. Mice were monitored twice
547 daily for changes in weight, ruffled fur, ataxia, and labored breathing for up to 14 days.
548 On days 1, 2 and 3, mice were anesthetized with isoflurane and throats were swabbed
549 with rayon-tipped swabs (Puritan, Fisher Scientific, Fisher Scientific, Waltham, MA). The
550 process for swabbing was constant across all treatment groups. Swabs were vortexed
551 briefly in 400 µL of Dulbecco's Modified Eagles Medium (DMEM, Fisher Scientific,
552 Waltham, MA) and frozen at -80°C. Mice were euthanized prior to experimental
553 endpoint if weight loss exceeded 20% of the starting weight or if animals were deemed
554 moribund as evidenced by limb weakness, ataxia or dragging of limbs, loss of limb
555 function or rapid or depressed respiration rate. An adverse event was defined as any

556 moribund disease signs at any time over the duration of the experiment. Prior to
557 euthanasia, whole blood was collected by submandibular vein puncture under isoflurane
558 anesthesia. Whole blood was clotted for >10 min at room temperature then centrifuged
559 for 5 minutes at 8,000 x g and cleared serum was stored at -80°C. Mice were
560 euthanized by isoflurane overdose and cervical dislocation then perfused with cold
561 sterile PBS. Lung (right inferior lobe) and brain (left hemisphere) were weighed and
562 homogenized in 1-10 µL/mg DMEM with a sterile glass bead at 30 Hz for 4 minutes
563 using a TissueLyser (Qiagen, Germantown, MD) automated homogenizer.
564 Homogenates were cleared by centrifugation at 10,000 x g for 4 minutes and the
565 cleared fraction was stored at -80°C.
566 ***Histopathology*:** At necropsy, lungs were inflated with 10% buffered formalin (Fisher
567 Scientific, Waltham, MA) and mice were fixed for 48 hours at room temperature in a 10-
568 fold volume of 10% buffered formalin. Skulls were demineralized in a 10-fold volume of
569 0.5 M ethylenediamine tetraacetic acid (EDTA) (pH=7) at 4°C for 14 days, with EDTA
570 solution exchanges every 3 days. Tissues were embedded in paraffin, thin-sectioned,
571 and stained with hematoxylin and eosin (H&E). H&E-stained slides were scanned by a
572 whole-slide image technique using an Aperio slide scanner (Leica, Buffalo Grove, IL)
573 with a resolution of 0.24 µm/pixel. Image files were uploaded on a Leica hosted web-
574 based site and a board certified veterinary anatomic pathologist without knowledge of
575 treatment conditions evaluated sections for SARS-CoV-2 induced histologic lesions. For
576 quantitative assessment of lung inflammation, digital images were captured and
577 analyzed using ImageJ software (Fiji, NIH) to estimate the area of inflamed tissue that
578 was visible to the naked eye at subgross magnification as a percentage of the total

579 surface area of the lung section. Each lung section was scored as described
580 (**Supplementary Table 2**).
581 **Fluorescent labeled tracing of GC in the nasal cavity**: FITC-labeled GC at a
582 concentration of 0.75% (7.5 mg/ml) was applied i.n. in 40 µL to female and male
583 wildtype C57BL/6 mice aged 6-8 weeks (Jackson Laboratories). FITC-GC was
584 manufactured by Immunophotonics, LLC. At 2h, 9h, 2d and 3d (where the last group
585 was administered FITC-GC one additional time 1d before euthanasia) after application,
586 2 mice per time were euthanized. Two additional mice were not FITC-GC treated; these
587 served as negative controls. The anterior half of the cranium was harvested as
588 described[72] and placed into 4% paraformaldehyde (Cat. 157-8-100, Electron
589 Microscopy Sciences) for 24 h at room temperature. Samples were sent to the St. Louis
590 University (SLU) histology core for processing. The samples were decalcified in
591 ImmunoCal for 2 weeks with the solution changed every 3 days. Next they were washed
592 with PBS then processed into paraffin and embedded. The sections were taken at 4.5
593 µm every 200 µm. The stained slides were scanned at 20x on an Olympus VS120 to
594 detect the FITC signal. For the unstained slides that were scanned, they first were
595 deparaffinized, then dehydrated so they could be coverslipped and scanned, and 5 µm
596 sections were taken every 200 µm and placed on a slide for examination under an
597 epifluorescence microscope to detect the FITC signal. Nasal concha were evaluated
598 histopathologically and measurements of fluorescence were performed using ImageJ
599 (Fiji). Briefly, images were standardized using the FITC Green channel with rendering
600 set to 1500 for optimal contrast. Screenshots of each micrograph were taken, and the
601 total area of nasal cavity and mucosa was traced and recorded. Teeth, oral mucosa,

602 and connective tissues were excluded for consistency, as sections were variably cut.
603 Fluorescent foci were traced and recorded. Percent area affected was calculated for
604 each slide as total fluorescent area divided by total nasal cavity area. Two sets of
605 measurements were taken per individual, with 4 total observations per treatment since 2
606 mice were included in each treatment group.
607 ***Plaque Assay*:** Washes from tracheal swabs, serum, residual inocula, and lung and
608 brain homogenates were thawed and assayed. Samples were serially diluted 10-fold in
609 DMEM with 1% bovine serum albumen (BSA) starting at an initial dilution of 1:8. 125 µL
610 of each dilution was added to confluent Vero CCL-81 cells (ATCC, Manassas, VA) in
611 12-well plates with cell culture media decanted. Virus was incubated on cells for 1 hour
612 at 5% CO2 in a humidified 37°C incubator. Cell monolayers were overlaid with 0.5%
613 agarose dissolved in DMEM with 5% fetal bovine serum (FBS) and 1x antibiotic-
614 antimycotic (Fisher Scientific, Waltham, MA) and incubated for 3 days at 5% CO2 and
615 37°C in a humidified incubator. Cells were fixed for >30 minutes with 4% formaldehyde
616 then agarose plugs were removed. Cells were stained with 0.05% crystal violet in 20%
617 ethanol for 10 minutes then rinsed three times with water. Plates were inverted to dry
618 completely and the number of plaques in each well was counted. Viral titers were
619 recorded as the reciprocal of the highest dilution where plaques were noted and are
620 represented as PFU per swab or PFU per mg of solid tissue.
621 ***Plaque Reduction Neutralization Test*:** Serum collected from mice at day 14 post
622 inoculation was thawed at 37°C and 30 µL was heated in a water bath for 30 minutes at
623 56°C to inactivate complement proteins. Serum was diluted 4-fold with virus diluent
624 consisting of PBS and 1% FBS, then samples were serially 2-fold diluted 11 times for a

625 dynamic range of 1:4 to 1:4096. An equal volume of virus diluent containing 80 PFU of
626 SARS-CoV-2 was added to each antibody dilution and a no-antibody control consisting
627 of virus diluent only, resulting in a final dynamic range of 1:4 to 1:8192 with one no-
628 antibody control. Antibody-virus dilution series were incubated for 1 hour at 37°C after
629 which they were applied to confluent Vero CCL-81 cells in single-replicate and
630 incubated for 1 hour at 5% CO2 and 37°C in a humidified incubator. Cells were overlaid,
631 incubated, fixed, and stained as described above for plaque assays. Neutralizing titer is
632 defined as the reciprocal of the dilution for which fewer than 20% of plaques were
633 detected versus the no-antibody control (>80% neutralization).
634 ***Statistics*:** All statistical tests were performed with GraphPad PRISM 9.0.2 (GraphPad
635 Software). Mann Whitney tests were used to compare cumulative pulmonary histologic
636 lesion scores in GC or PBS treated mice. Logrank (Mantel-Cox) test for survival
637 proportions were performed pairwise and *p*-values were adjusted with Bonferroni
638 correction using R version 4.0.0 (R Project) p.adjust function. The correlation between
639 mortality and positive virus detection was calculated by Fisher's exact test. Repeated
640 measures two-way ANOVA tests were performed on log10-transformed viral titers and
641 multiple comparisons were computed according to Tukey method. Main effect two-way
642 ANOVA tests were performed on mouse weights normalized to starting values at the
643 time of virus inoculation or log10-transformed viral titers and multiple comparisons were
644 computed with Tukey's method. Area under the curve (AUC) was calculated for
645 longitudinally collected tracheal swabs from days 1,2 and 3 and log10-transformed.
646 ANOVA of grouped log10-AUC was performed with multiple comparisons computed
647 with Tukey's method. ANOVA was performed on untransformed histologic scores or

648 percentage of lung affected by inflammation and multiple comparisons were computed
649 with Bonferroni's method. A Kruskal-Wallis H test was performed on untransformed
650 PRNT80 neutralization values and multiple comparisons were computed according to
651 Dunn's method.
652
653 **DATA AVAILABILITY**
654 All data contributing to the generation of figures and analyses described herein are
655 available at 10.5281/zenodo.7709464.
656
657 **COMPETING INTERESTS**
658 TH, CFW, SSKL declare a conflict of interest as employees with minority ownership
659 stakes of Immunophotonics, Inc., the manufacturer of the proprietary immune stimulant
660 GC. RML declares a conflict of interest as an advisor with minority ownership stake in
661 Immunophotonics.
662
663 **AUTHOR CONTRIBUTIONS**
664 Conceptualization: RML, LLC, TH, SSKL, CMW, HL, ARH, and EEB. Investigation:
665 CMW, HL, EEB, ARH, TSW, CFW, EEV. Writing draft: CMW. Review and editing:
666 CMW, HL, EEB, LLC, TH, SSKL, MKK, RML, ARH, TSW, WRC. Visualization: CMW,
667 EEB, MKK, TSW, LLC. Supervision and project administration: LLC, WRC. Funding
668 acquisition: RML, LLC, WRC.
669
670 **ACKNOWLEDGEMENTS**

Funding support was provided by the UC Berkeley Henry Wheeler Center for Emerging and Neglected Diseases (CEND) COVID Catalyst Fund, and internal funding from the UC Davis Office of the Vice Chancellor of Research. Funding sources did not influence experimental design and analysis/interpretation of results or impact the decision to publish.

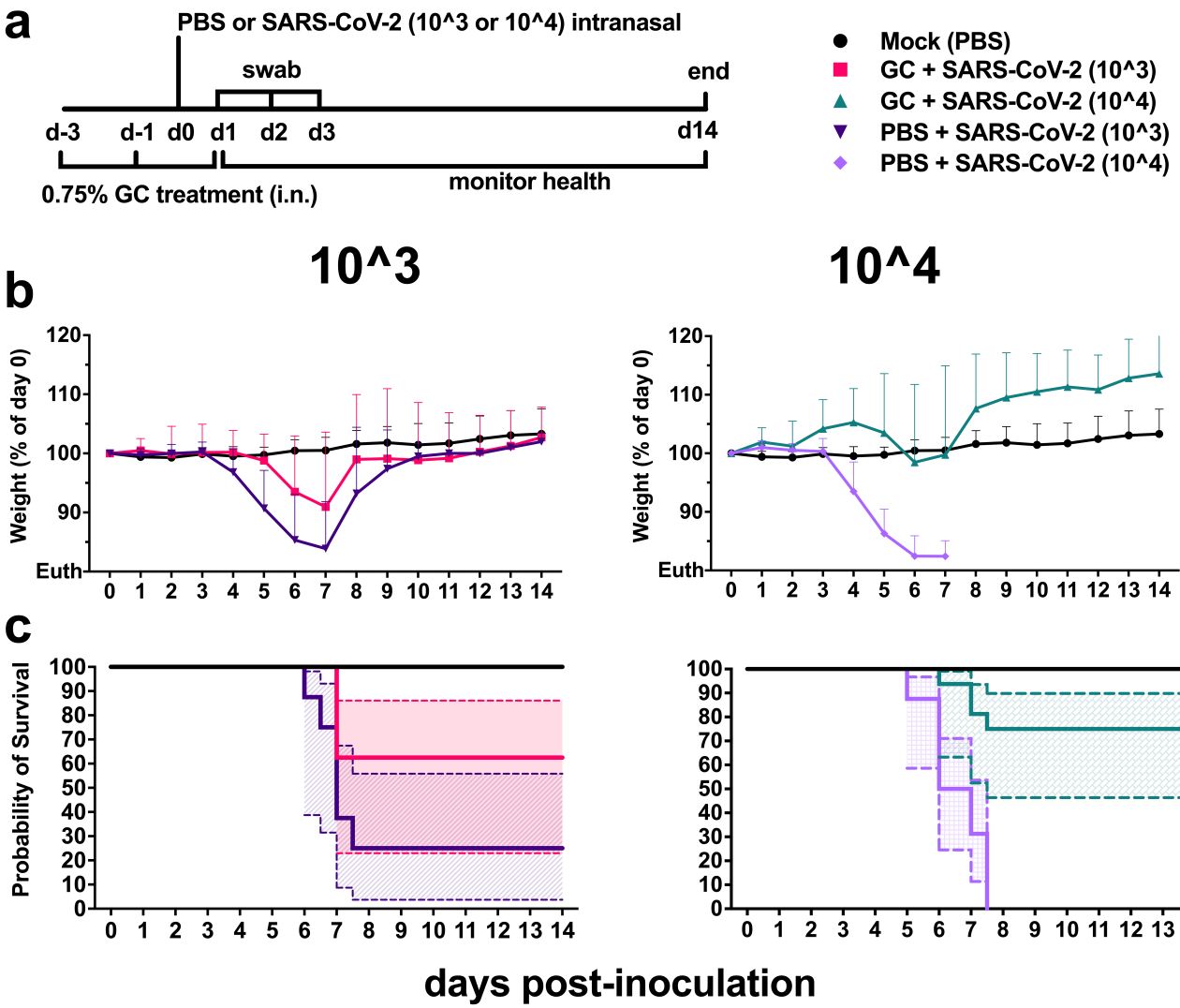

d Survival comparisons

GROUP 1	GROUP 2	P VALUE	SIGNIFICANCE
mock	GC + SARS-CoV-2 (10^3)	0.5024	ns
mock	GC + SARS-CoV-2 (10^4)	1.0000	ns
mock	SARS-CoV2 (10^3)	0.0200	*
mock	SARS-CoV-2 (10^4)	0.0001	****
GC + SARS-CoV-2 (10^3)	GC + SARS-CoV-2 (10^4)	1.0000	ns
GC + SARS-CoV-2 (10^3)	SARS-CoV2 (10^3)	0.0504	ns
GC + SARS-CoV-2 (10^4)	SARS-CoV-2 (10^4)	0.0001	****
SARS-CoV2 (10^3)	SARS-CoV-2 (10^4)	1.0000	ns

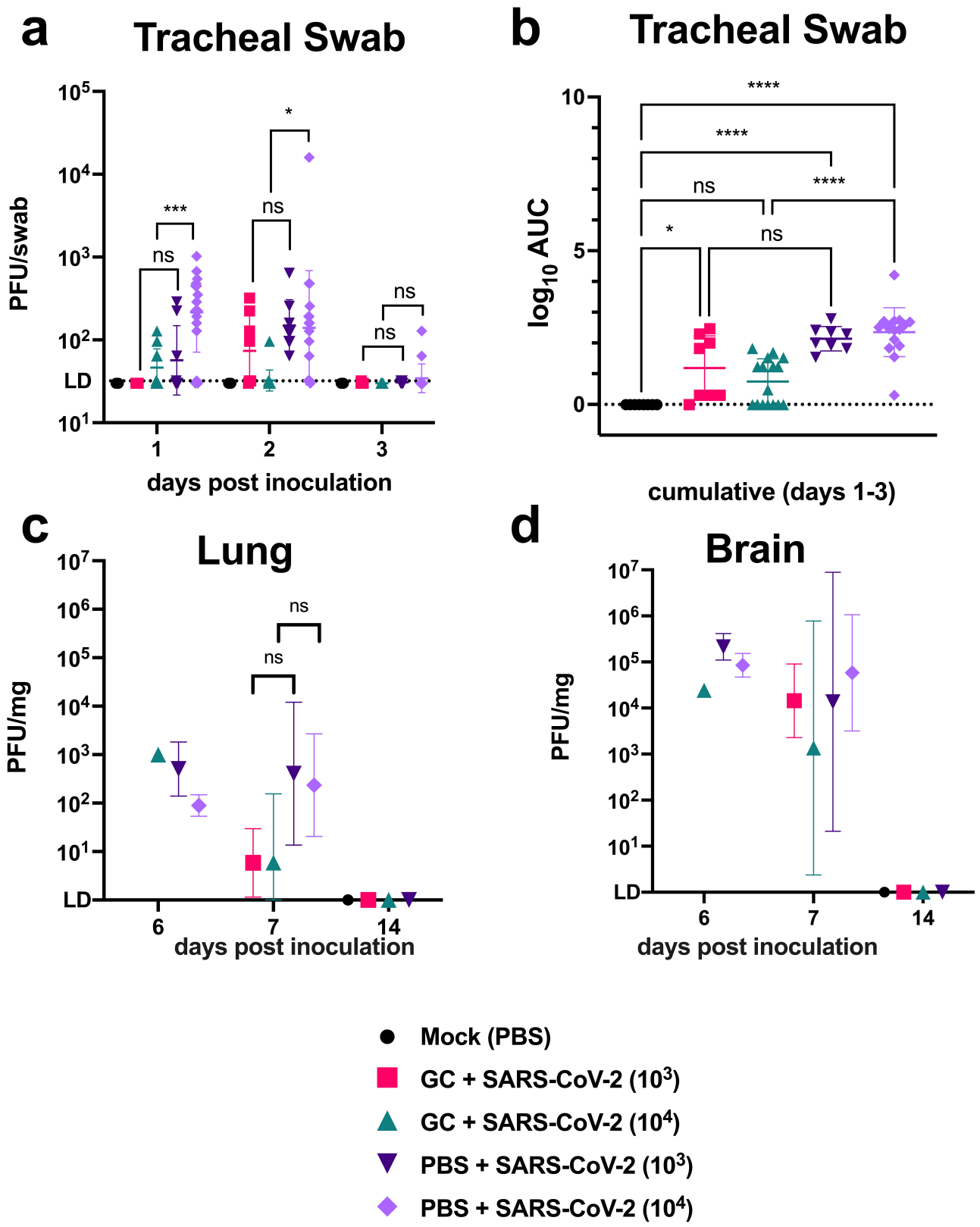
a
Tracheal Swab
PFU/swab
10^5
10^4
10^3
10^2
LD
10^1
***
ns
*
ns
ns
ns
1
2
3
days post inoculation
b
Tracheal Swab
$\log_{10}$ AUC
10
5
0
****
****
****
ns
ns
*
cumulative (days 1-3)
c
Lung
PFU/mg
10^7
10^6
10^5
10^4
10^3
10^2
10^1
LD
ns
ns
6
7
14
days post inoculation
d
Brain
PFU/mg
10^7
10^6
10^5
10^4
10^3
10^2
10^1
LD
6
7
14
days post inoculation
Mock (PBS)
GC + SARS-CoV-2 (10^3)
GC + SARS-CoV-2 (10^4)
PBS + SARS-CoV-2 (10^3)
PBS + SARS-CoV-2 (10^4)

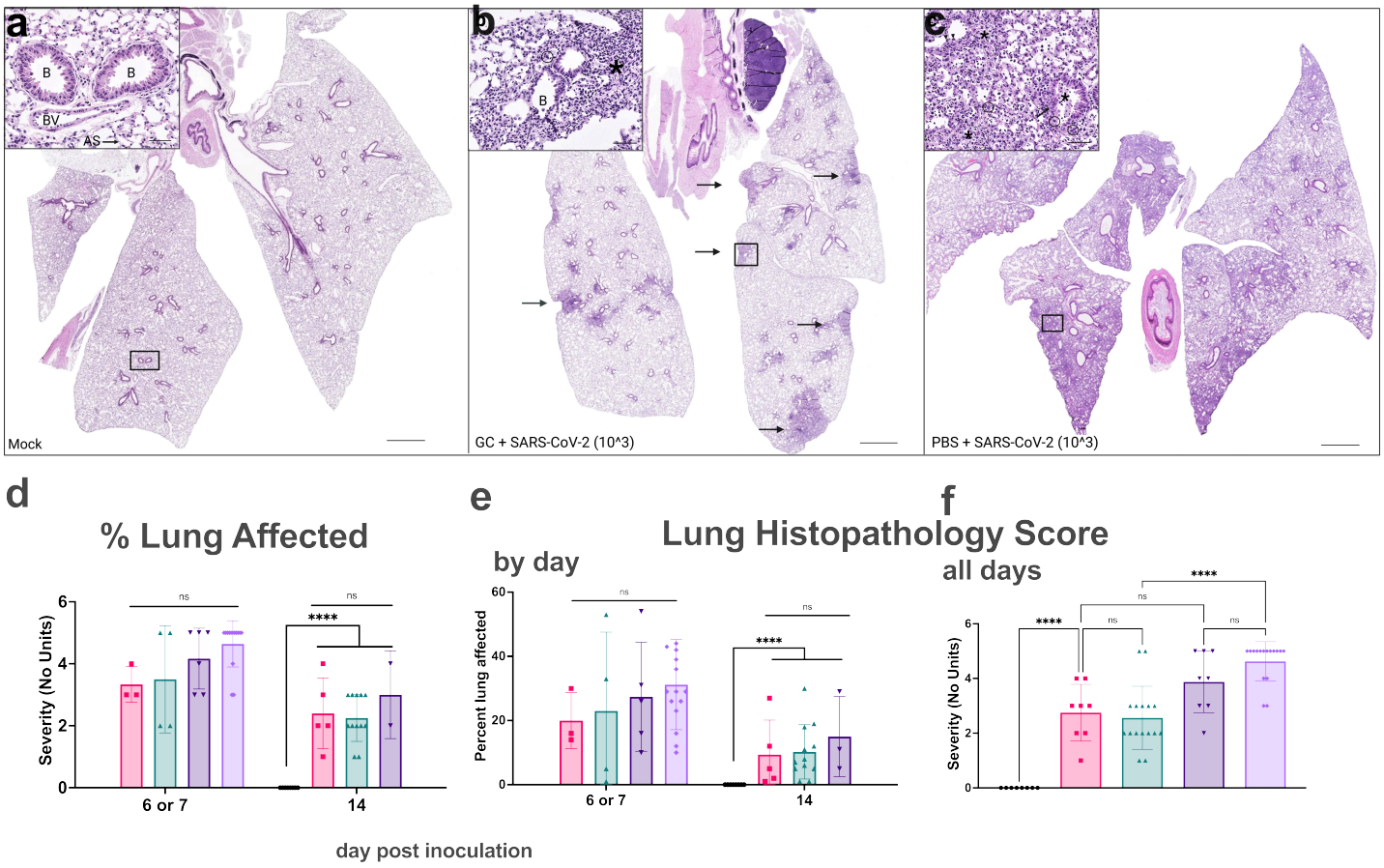
a
B
B
BV
AS
Mock
b
B
GC + SARS-CoV-2 (10^3)
c
PBS + SARS-CoV-2 (10^3)
d
% Lung Affected
Severity (No Units)
ns
****
6 or 7
14
e
Lung Histopathology Score
by day
Percent lung affected
ns
****
6 or 7
14
f
all days
Severity (No Units)
****
ns
ns
ns
day post inoculation
Mock (PBS)
GC + SARS-CoV-2 (10^3)
GC + SARS-CoV-2 (10^4)
PBS + SARS-CoV-2 (10^3)
PBS + SARS-CoV-2 (10^4)

PRNT80

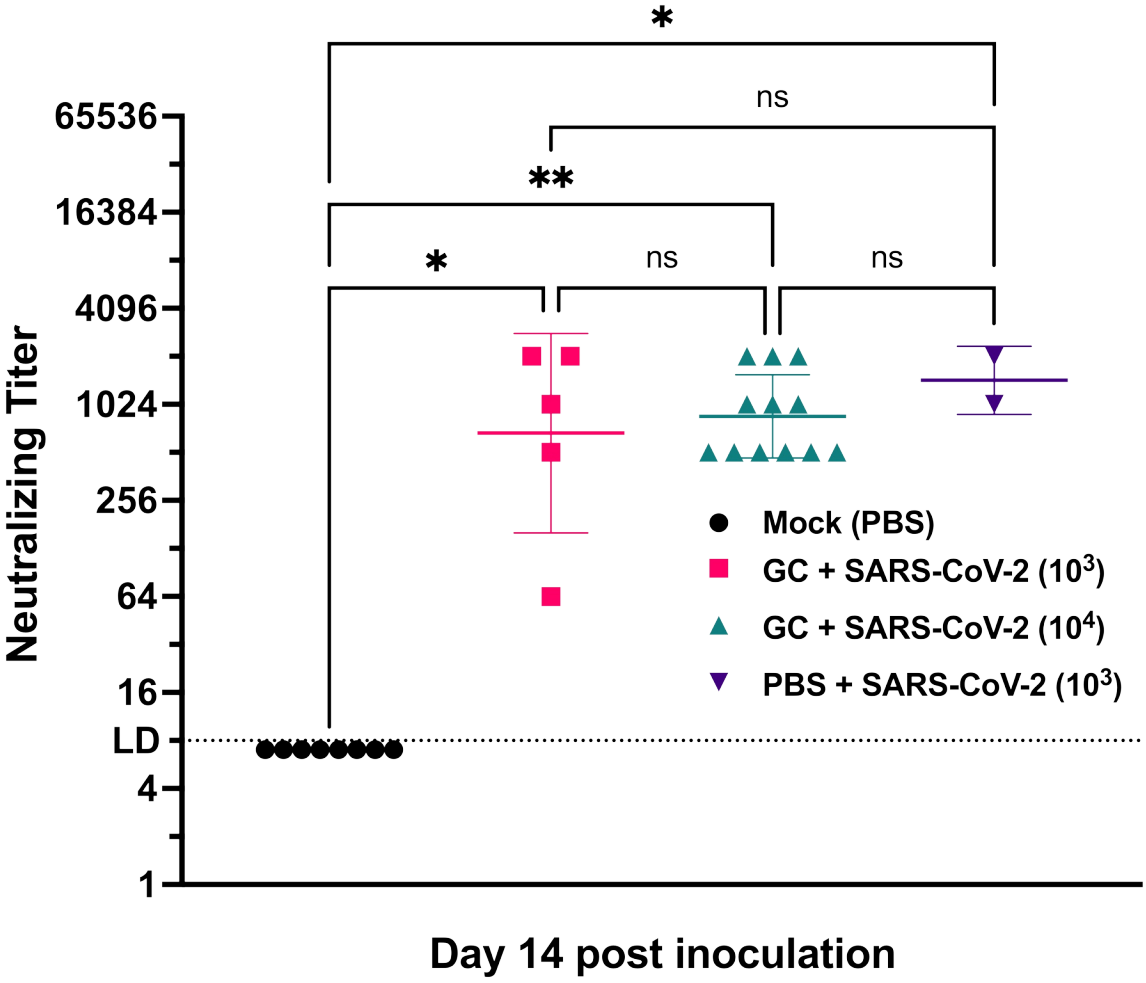
*
ns
**
*
ns
ns
65536
16384
4096
1024
256
64
16
LD
4
1
Neutralizing Titer
Mock (PBS)
GC + SARS-CoV-2 (10^3)
GC + SARS-CoV-2 (10^4)
PBS + SARS-CoV-2 (10^3)
Day 14 post inoculation

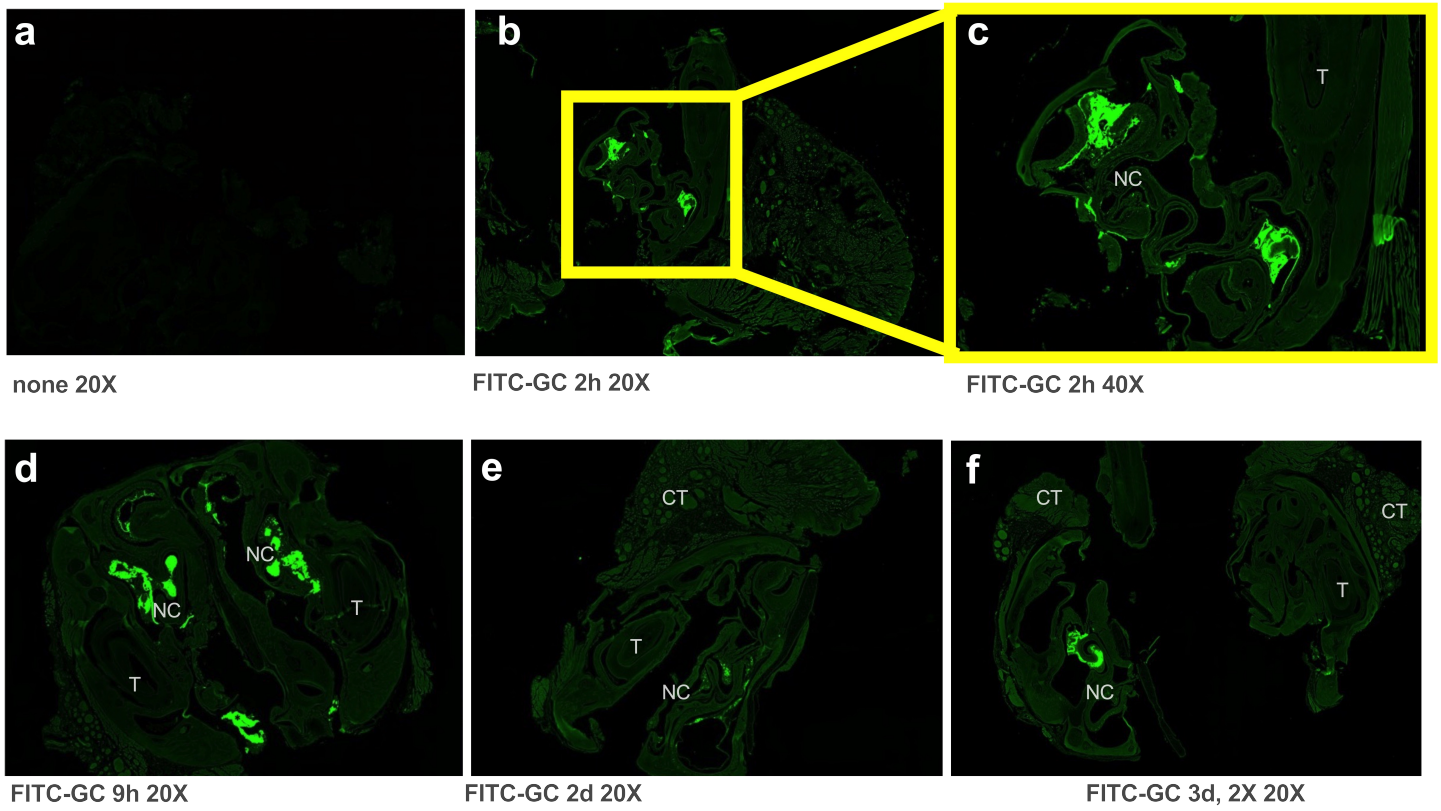
a
b
c
T
NC
none 20X
FITC-GC 2h 20X
FITC-GC 2h 40X
d
e
f
NC
NC
T
T
CT
T
NC
CT
CT
T
NC
FITC-GC 9h 20X
FITC-GC 2d 20X
FITC-GC 3d, 2X 20X

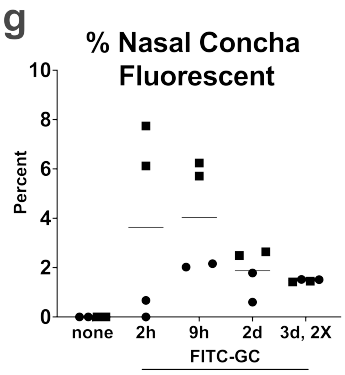
g
% Nasal Concha Fluorescent
Percent
10
8
6
4
2
0
none
2h
9h
2d
3d, 2X
FITC-GC

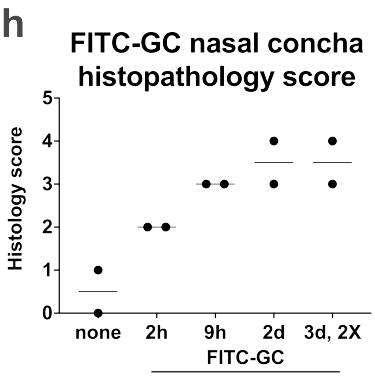
h
FITC-GC nasal concha histopathology score
Histology score
5
4
3
2
1
0
none
2h
9h
2d
3d, 2X
FITC-GC

677

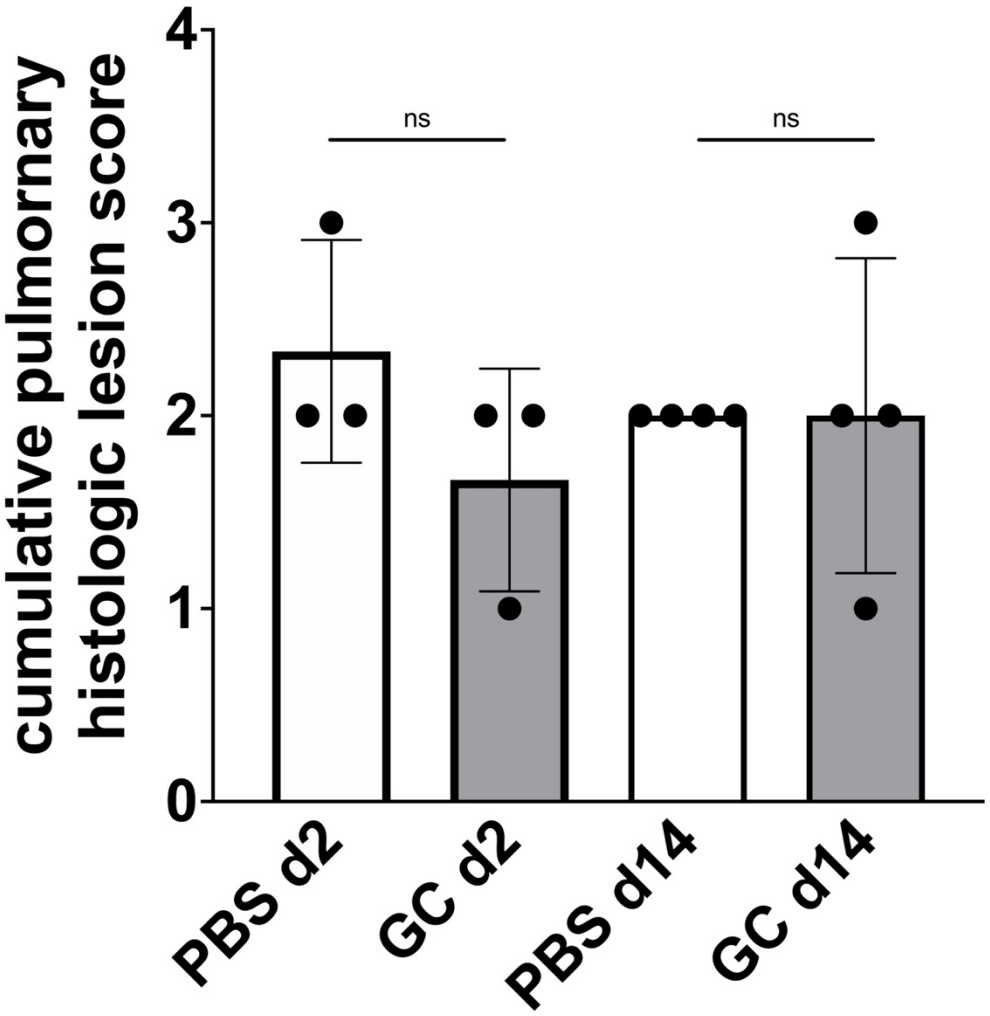

678
679 **Supplementary Fig. 1**. **GC administered intranasally does not produce**
680 **histopathologic changes in murine lung tissues**. Six-week-old male and female
681 mice were treated intranasally at 3 intervals with GC or PBS following the same
682 schedule used for mice in the SARS-CoV-2 cohorts. Mice were euthanized 2 or 14 days
683 after the last treatment. Cumulative lung lesion scores were determined using the
684 scoring scale in Supplementary Table 2. A comprehensive list of lesions detected in
685 each animal is shown in Supplementary Table 2. ns is not significant, Mann Whitney
686 test (P=0.6).

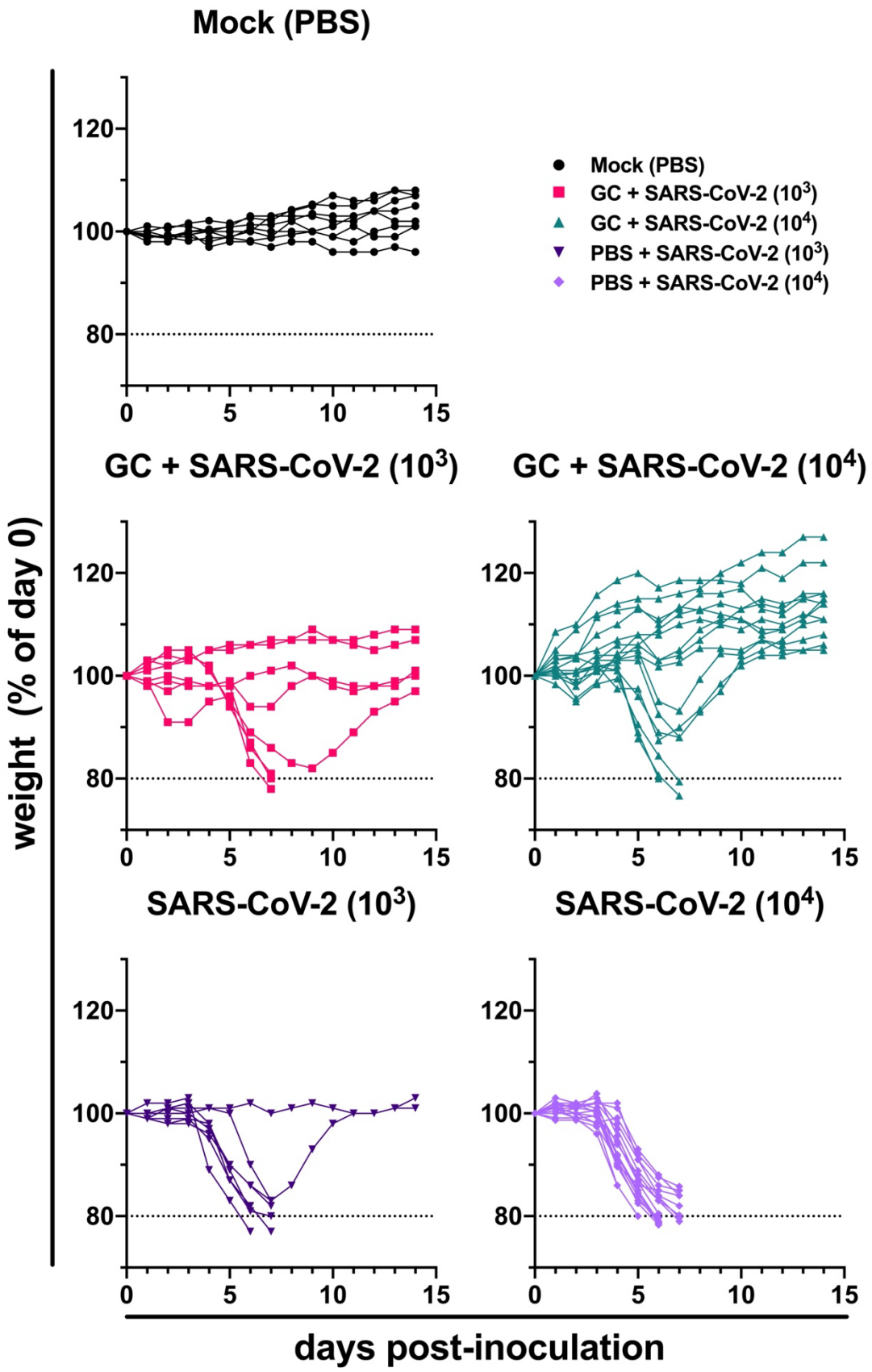
Mock (PBS)
GC + SARS-CoV-2 (10^3)
GC + SARS-CoV-2 (10^4)
SARS-CoV-2 (10^3)
SARS-CoV-2 (10^4)
Mock (PBS)
GC + SARS-CoV-2 (10^3)
GC + SARS-CoV-2 (10^4)
PBS + SARS-CoV-2 (10^3)
PBS + SARS-CoV-2 (10^4)
weight (% of day 0)
days post-inoculation
120
100
80
0
5
10
15

687

688 **Supplementary Fig. 2: N-dihydrogalactochitosan protects mice from SARS-CoV-2**

689 **weight loss.** Each line shows individual mouse weight as a percentage of their starting

690 weight at the time of inoculation.

691

692

693 **Supplementary Table 2: Lung histopathology scoring criteria.**

Score		Description
0	none	Within normal limits or rare, scattered lymphocytic infiltrates not observed in control animals but significance questionable (could be background lesion or variation of normal).
1	minimal	Minimal mononuclear inflammation affecting less than 2% of the section. Inflammatory leukocyte infiltration is limited to a perivascular and/or peribronchiolar distribution with no evidence of alveolar or vascular injury.
2	mild	Mild peribronchiolar/perivascular inflammation which may also expand alveoli/alveolar septa, composed primarily of macrophages and lymphocytes (+/- scattered neutrophils); increased alveolar macrophages; alveolar septal architecture largely intact; affects 2-10% of the section; and/or scattered alveolar hemorrhage/fibrin/edema; and/or scattered atypical/multinucleated syncytial cells.
3	moderate	Moderate bronchointerstitial and perivascular inflammation, increased alveolar macrophages, and/or alveolar hemorrhage/fibrin/edema (characterized as above); and/or alveolar damage (characterized by type I pneumocyte necrosis or loss with replacement by hyaline membranes, fibrin, edema, and/or necrotic debris); and/or reparative/regenerative changes (type II pneumocyte hyperplasia, atypical/multinucleated syncytial cells, or fibrosis); lesions affect 10-25% of the section.
4	severe	As above but more widespread inflammation, hemorrhage/fibrin/ edema, and/or alveolar damage/loss of normal septal architecture; and or regenerative changes affecting greater than 25% of the section.
+1		Add 1 point if: Greater than 25% of inflammatory cells are neutrophils; there is significant necrotizing vasculitis, endotheliitis or microthrombi; or if there is

		significant bronchiolitis, airway epithelial necrosis or hyperplasia.

694

695

696

697 **Supplementary Table 3: Nasal concha histopathology scoring criteria.**

Score	Degree	Nasal Cavity
0	none	Within normal limits or rare, scattered lymphocytic infiltrates and/or rare foci of mucus, proteinaceous fluid, sloughed epithelium and/or free RBCs not observed in control animals but significance questionable (could be background lesion or variation of normal)
1	minimal	As above with minimal mononuclear submucosal and/or perivascular inflammation
2	mild	Mild rhinitis characterized by mucosal/submucosal primarily mononuclear inflammation (+/- low numbers of neutrophils) which may extend into the nasal cavity (along with sloughed epithelial cells and small amounts of mucus/fibrin); overall normal/intact nasal architecture.
3	moderate	Moderate rhinitis characterized by a mixed inflammatory mucosal/submucosal infiltrate and/or nasal cavity exudate composed of neutrophils, macrophages, and lymphocytes +/- mild to moderate hemorrhage, fibrin, edema and/or necrotic debris.
4	severe	As above but with more widespread and severe inflammation and/or mucosal erosion/necrosis.

698
699
700
701
702
703
704
705
706
707

REFERENCES

1. Huang C, Wang Y, Li X, Ren L, Zhao J, Hu Y, et al. Clinical features of patients infected with 2019 novel coronavirus in Wuhan, China. The Lancet. 2020. doi:10.1016/S0140-6736(20)30183-5
2. COVID-19 Map - Johns Hopkins Coronavirus Resource Center. [cited 6 Mar 2023]. Available: https://coronavirus.jhu.edu/map.html
3. Wang D, Hu B, Hu C, Zhu F, Liu X, Zhang J, et al. Clinical Characteristics of 138 Hospitalized Patients with 2019 Novel Coronavirus-Infected Pneumonia in Wuhan, China. JAMA - Journal of the American Medical Association. 2020;323: 1061–1069. doi:10.1001/jama.2020.1585
4. Chen N, Zhou M, Dong X, Qu J, Gong F, Han Y, et al. Epidemiological and clinical characteristics of 99 cases of 2019 novel coronavirus pneumonia in Wuhan, China: a descriptive study. The Lancet. 2020;395: 507–513. doi:10.1016/S0140-6736(20)30211-7
5. Zhou F, Yu T, Du R, Fan G, Liu Y, Liu Z, et al. Clinical course and risk factors for mortality of adult inpatients with COVID-19 in Wuhan, China: a retrospective cohort study. The Lancet. 2020;395: 1054–1062. doi:10.1016/S0140-6736(20)30566-3
6. Hellmuth J, Barnett TA, Asken BM, Kelly JD, Torres L, Stephens ML, et al. Persistent COVID-19-associated neurocognitive symptoms in non-hospitalized patients. J Neurovirol. 2021;27: 191–195. doi:10.1007/s13365-021-00954-4
7. Graham EL, Clark JR, Orban ZS, Lim PH, Szymanski AL, Taylor C, et al. Persistent neurologic symptoms and cognitive dysfunction in non-hospitalized Covid-19 “long haulers.” Ann Clin Transl Neurol. 2021. doi:10.1002/acn3.51350
8. Lu R, Zhao X, Li J, Niu P, Yang B, Wu H, et al. Genomic characterisation and epidemiology of 2019 novel coronavirus: implications for virus origins and receptor binding. The Lancet. 2020;395: 565–574. doi:10.1016/S0140-6736(20)30251-8
9. Zhou P, Yang X Lou, Wang XG, Hu B, Zhang L, Zhang W, et al. A pneumonia outbreak associated with a new coronavirus of probable bat origin. Nature. 2020;579: 270–273. doi:10.1038/s41586-020-2012-7
10. Lakdawala SS, Menachery VD. The search for a COVID-19 animal model. Science (1979). 2020;368: 942–943. doi:10.1126/science.abc6141
11. Muñoz-Fontela C, Dowling WE, Funnell SGP, Gsell PS, Riveros-Balta AX, Albrecht RA, et al. Animal models for COVID-19. Nature. 2020;586: 509–515. doi:10.1038/s41586-020-2787-6
12. McCray PB, Pewe L, Wohlford-Lenane C, Hickey M, Manzel L, Shi L, et al. Lethal Infection of K18-hACE2 Mice Infected with Severe Acute Respiratory Syndrome Coronavirus. J Virol. 2007. doi:10.1128/jvi.02012-06
13. Winkler ES, Bailey AL, Kafai NM, Nair S, McCune BT, Yu J, et al. SARS-CoV-2 infection of human ACE2-transgenic mice causes severe lung

753 inflammation and impaired function. Nat Immunol. 2020;21: 1327–1335.
754 doi:10.1038/s41590-020-0778-2
755 14. Zheng J, Wong LYR, Li K, Verma AK, Ortiz ME, Wohlford-Lenane C, et al.
756 COVID-19 treatments and pathogenesis including anosmia in K18-hACE2
757 mice. Nature. 2021;589: 603–607. doi:10.1038/s41586-020-2943-z
758 15. Symptoms of COVID-19 | CDC. [cited 21 May 2021]. Available:
759 https://www.cdc.gov/coronavirus/2019-ncov/symptoms-
760 testing/symptoms.html
761 16. FDA Issues Emergency Use Authorization for Third COVID-19 Vaccine |
762 FDA. [cited 26 Apr 2021]. Available: https://www.fda.gov/news-
763 events/press-announcements/fda-issues-emergency-use-authorization-
764 third-covid-19-vaccine
765 17. Coronavirus disease (COVID-19): Herd immunity, lockdowns and COVID-
766 19. [cited 26 Apr 2021]. Available: https://www.who.int/news-room/q-a-
767 detail/herd-immunity-lockdowns-and-covid-19
768 18. Rhoades A. Veklury (remdesivir) EUA Letter of Approval, reissued
769 10/22/2020. 2020.
770 19. Beigel JH, Tomashek KM, Dodd LE, Mehta AK, Zingman BS, Kalil AC, et al.
771 Remdesivir for the Treatment of Covid-19 — Final Report. New England
772 Journal of Medicine. 2020;383: 1813–1826. doi:10.1056/NEJMoa2007764
773 20. WHO recommends against the use of remdesivir in COVID-19 patients.
774 [cited 25 Apr 2021]. Available: https://www.who.int/news-room/feature-
775 stories/detail/who-recommends-against-the-use-of-remdesivir-in-covid-19-
776 patients
777 21. Administration D. FDA Combating COVID-19 With Therapeutics. 2020.
778 22. Emergency Use Authorization | FDA. [cited 7 Mar 2023]. Available:
779 https://www.fda.gov/emergency-preparedness-and-response/mcm-legal-
780 regulatory-and-policy-framework/emergency-use-authorization#coviddrugs
781 23. Chirkov SN. The antiviral activity of chitosan (review). Applied Biochemistry
782 and Microbiology. 2002. pp. 1–8. doi:10.1023/A:1013206517442
783 24. Mehrabi M, Montazeri H, Dounighi MN, Rashti A, Vakili-Ghartavol R.
784 Chitosan-based nanoparticles in mucosal vaccine delivery. Archives of Razi
785 Institute. Razi Vaccine and Serum Research Institute; 2018. pp. 165–176.
786 doi:10.22092/ari.2017.109235.1101
787 25. Li X, Min M, Du N, Gu Y, Hode T, Naylor M, et al. Chitin, chitosan, and
788 glycated chitosan regulate immune responses: The novel adjuvants for
789 cancer vaccine. Clinical and Developmental Immunology. Hindawi Limited;
790 2013. doi:10.1155/2013/387023
791 26. Mudgal J, Mudgal PP, Kinra M, Raval R. Immunomodulatory role of
792 chitosan-based nanoparticles and oligosaccharides in cyclophosphamide-
793 treated mice. Scand J Immunol. 2019;89: e12749. doi:10.1111/sji.12749
794 27. Carroll TD, Jegaskanda S, Matzinger SR, Fritts L, McChesney MB, Kent SJ,
795 et al. A lipid/DNA adjuvant-inactivated influenza virus vaccine protects
796 rhesus macaques from uncontrolled virus replication afer heterosubtypic
797 influenza a virus challenge. Journal of Infectious Diseases. 2018.
798 doi:10.1093/infdis/jiy238

28. Lei X, Dong X, Ma R, Wang W, Xiao X, Tian Z, et al. Activation and evasion of type I interferon responses by SARS-CoV-2. Nat Commun. 2020;11. doi:10.1038/s41467-020-17665-9
29. Xia H, Cao Z, Xie X, Zhang X, Chen JYC, Wang H, et al. Evasion of Type I Interferon by SARS-CoV-2. Cell Rep. 2020;33. doi:10.1016/j.celrep.2020.108234
30. Ribero MS, Jouvenet N, Dreux M, Nisole S. Interplay between SARS-CoV-2 and the type I interferon response. PLoS Pathogens. Public Library of Science; 2020. doi:10.1371/journal.ppat.1008737
31. Zheng M, Qu D, Wang H, Sun Z, Liu X, Chen J, et al. Intranasal Administration of Chitosan Against Influenza A (H7N9) Virus Infection in a Mouse Model. Sci Rep. 2016;6. doi:10.1038/srep28729
32. Wang X, Zhang W, Liu F, Zheng M, Zheng D, Zhang T, et al. Intranasal immunization with live attenuated influenza vaccine plus chitosan as an adjuvant protects mice against homologous and heterologous virus challenge. Arch Virol. 2012;157: 1451–1461. doi:10.1007/s00705-012-1318-7
33. Choi B, Jo DH, Anower AKMM, Islam SMS, Sohn S. Chitosan as an Immunomodulating Adjuvant on T-Cells and Antigen-Presenting Cells in Herpes Simplex Virus Type 1 Infection. Mediators Inflamm. 2016;2016. doi:10.1155/2016/4374375
34. Pyrć K, Milewska A, Duran EB, Botwina P, Dabrowska A, Jedrysik M, et al. SARS-CoV-2 inhibition using a mucoadhesive, amphiphilic chitosan that may serve as an anti-viral nasal spray. Sci Rep. 2021;11. doi:10.1038/s41598-021-99404-8
35. Jaber N, Al-Remawi M, Al-Akayleh F, Al-Muhtaseb N, Al-Adham ISI, Collier PJ. A review of the antiviral activity of Chitosan, including patented applications and its potential use against COVID-19. J Appl Microbiol. 2022;132: 41–58. doi:10.1111/jam.15202
36. Safarzadeh M, Sadeghi S, Azizi M, Rastegari-Pouyani M, Pouriran R, Haji Molla Hoseini M. Chitin and chitosan as tools to combat COVID-19: A triple approach. Int J Biol Macromol. 2021;183: 235–244. doi:10.1016/j.ijbiomac.2021.04.157
37. Sharma N, Modak C, Singh PK, Kumar R, Khatri D, Singh SB. Underscoring the immense potential of chitosan in fighting a wide spectrum of viruses: A plausible molecule against SARS-CoV-2? Int J Biol Macromol. 2021;179: 33–44. doi:10.1016/j.ijbiomac.2021.02.090
38. Zhuo S-H, Wu J-J, Zhao L, Li W-H, Zhao Y-F, Li Y-M. A chitosan-mediated inhalable nanovaccine against SARS-CoV-2. Nano Res. 2022;15: 4191–4200. doi:10.1007/s12274-021-4012-9
39. Tan RSL, Hassandarvish P, Chee CF, Chan LW, Wong TW. Chitosan and its derivatives as polymeric anti-viral therapeutics and potential anti-SARS-CoV-2 nanomedicine. Carbohydr Polym. 2022;290: 119500. doi:10.1016/j.carbpol.2022.119500
40. Chen WR, Carubelli R, Liu H, Nordquist RE. Laser immunotherapy: A novel treatment modality for metastatic tumors. Applied Biochemistry and

845 Biotechnology - Part B Molecular Biotechnology. 2003;25: 37–43.
846 doi:10.1385/MB:25:1:37
847 41. Song S, Zhou F, Nordquist RE, Carubelli R, Liu H, Chen WR. Glycated
848 chitosan as a new non-toxic immunological stimulant Glycated chitosan
849 immunological stimulant. Immunopharmacol Immunotoxicol. 2009;31: 202–
850 208. doi:10.1080/08923970802629593
851 42. Zizzari I, Napoletano C, Battisti F, Rahimi H, Caponnetto S, Pierelli L, et al.
852 MGL Receptor and Immunity: When the Ligand Can Make the Difference. J
853 Immunol Res. 2015;2015. doi:10.1155/2015/450695
854 43. Korbelik M, Banáth J, Zhang W, Hode T, Lam S, Gallagher P, et al. N-
855 dihydrogalactochitosan-supported tumor control by photothermal therapy
856 and photothermal therapy-generated vaccine. J Photochem Photobiol B.
857 2020;204. doi:10.1016/J.JPHOTOBIOL.2020.111780
858 44. Korbelik M, Hode T, Lam SSK, Chen WR. Novel Immune Stimulant
859 Amplifies Direct Tumoricidal Effect of Cancer Ablation Therapies and Their
860 Systemic Antitumor Immune Efficacy. Cells. NLM (Medline); 2021.
861 doi:10.3390/cells10030492
862 45. Qi S, Lu L, Zhou F, Chen Y, Xu M, Chen L, et al. Neutrophil infiltration and
863 whole-cell vaccine elicited by N-dihydrogalactochitosan combined with NIR
864 phototherapy to enhance antitumor immune response and T cell immune
865 memory. Theranostics. 2020;10: 1814–1832. doi:10.7150/thno.38515
866 46. Zhou F, Yang J, Zhang Y, Liu M, Lang ML, Li M, et al. Local phototherapy
867 synergizes with immunoadjuvant for treatment of pancreatic cancer through
868 induced immunogenic tumor vaccine. Clinical Cancer Research. 2018;24:
869 5335–5346. doi:10.1158/1078-0432.CCR-18-1126
870 47. El-Hussein A, Lam SSK, Raker J, Chen WR, Hamblin MR. N-
871 dihydrogalactochitosan as a potent immune activator for dendritic cells. J
872 Biomed Mater Res A. 2017;105: 963–972. doi:10.1002/jbm.a.35991
873 48. Hoover AR, Liu K, Devette CI, Krawic JR, West CL, Medcalf D, et al.
874 ScRNA-seq reveals tumor microenvironment remodeling induced by local
875 intervention-based immunotherapy. bioRxiv. 2020; 2020.10.02.323006.
876 doi:10.1101/2020.10.02.323006
877 49. Hoover AR, More S, Liu K, West CL, Valero TI, Yu N, et al. A novel
878 biopolymer for mucosal adjuvant against respiratory pathogens. bioRxiv.
879 2022; 2022.09.07.506979. doi:10.1101/2022.09.07.506979
880 50. Brown C, Vostok J, Johnson H, Burns M, Gharpure R, Sami S, et al.
881 Outbreak of SARS-CoV-2 Infections, Including COVID-19 Vaccine
882 Breakthrough Infections, Associated with Large Public Gatherings -
883 Barnstable County, Massachusetts, July 2021. MMWR Morb Mortal Wkly
884 Rep. 2021;70: 1059–1062. doi:10.15585/MMWR.MM7031E2
885 51. Bellich B, D'Agostino I, Semeraro S, Gamini A, Cesàro A. "The Good, the
886 Bad and the Ugly" of Chitosans. Mar Drugs. 2016;14.
887 doi:10.3390/MD14050099
888 52. Jayathilakan K, Sultana K, Radhakrishna K, Bawa AS. Utilization of
889 byproducts and waste materials from meat, poultry and fish processing

890 industries: A review. Journal of Food Science and Technology. J Food Sci
891 Technol; 2012. pp. 278–293. doi:10.1007/s13197-011-0290-7
892 53. Negm NA, Hefni HHH, Abd-Elaal AAA, Badr EA, Abou Kana MTH.
893 Advancement on modification of chitosan biopolymer and its potential
894 applications. International Journal of Biological Macromolecules. Elsevier
895 B.V.; 2020. pp. 681–702. doi:10.1016/j.ijbiomac.2020.02.196
896 54. Mokhtar H, Biffar L, Somavarapu S, Frossard JP, McGowan S, Pedrera M,
897 et al. Evaluation of hydrophobic chitosan-based particulate formulations of
898 porcine reproductive and respiratory syndrome virus vaccine candidate T
899 cell antigens. Vet Microbiol. 2017;209: 66–74.
900 doi:10.1016/j.vetmic.2017.01.037
901 55. Shim S, Park HE, Soh SH, Im Y Bin, Yoo HS. Induction of Th2 response
902 through TLR2-mediated MyD88-dependent pathway in human microfold
903 cells stimulated with chitosan nanoparticles loaded with Brucella abortus
904 Mdh. Microb Pathog. 2020;142. doi:10.1016/j.micpath.2020.104040
905 56. Zhang X, Wu K, Wang D, Yue X, Song D, Zhu Y, et al. Nucleocapsid
906 protein of SARS-CoV activates interleukin-6 expression through cellular
907 transcription factor NF-κB. Virology. 2007;365: 324–335.
908 doi:10.1016/j.virol.2007.04.009
909 57. Blanco-Melo D, Nilsson-Payant BE, Liu WC, Uhl S, Hoagland D, Møller R,
910 et al. Imbalanced Host Response to SARS-CoV-2 Drives Development of
911 COVID-19. Cell. 2020;181: 1036-1045.e9. doi:10.1016/j.cell.2020.04.026
912 58. Pyle C, Uwadiae F, Swieboda D, Harker J. Early IL-6 signalling promotes
913 IL-27 dependent maturation of regulatory T cells in the lungs and resolution
914 of viral immunopathology. PLoS Pathog. 2017;13.
915 doi:10.1371/JOURNAL.PPAT.1006640
916 59. Bueter CL, Lee CK, Rathinam VAK, Healy GJ, Taron CH, Specht CA, et al.
917 Chitosan but not chitin activates the inflammasome by a mechanism
918 dependent upon phagocytosis. Journal of Biological Chemistry. 2011;286:
919 35447–35455. doi:10.1074/jbc.M111.274936
920 60. Carroll EC, Jin L, Mori A, Muñoz-Wolf N, Oleszycka E, Moran HBT, et al.
921 The Vaccine Adjuvant Chitosan Promotes Cellular Immunity via DNA
922 Sensor cGAS-STING-Dependent Induction of Type I Interferons. Immunity.
923 2016;44: 597–608. doi:10.1016/j.immuni.2016.02.004
924 61. Sun B, Yu S, Zhao D, Guo S, Wang X, Zhao K. Polysaccharides as vaccine
925 adjuvants. Vaccine. Elsevier Ltd; 2018. pp. 5226–5234.
926 doi:10.1016/j.vaccine.2018.07.040
927 62. Read RC, Naylor SC, Potter CW, Bond J, Jabbal-Gill I, Fisher A, et al.
928 Effective nasal influenza vaccine delivery using chitosan. Vaccine. 2005;23:
929 4367–4374. doi:10.1016/j.vaccine.2005.04.021
930 63. Elieh Ali Komi D, Sharma L, Dela Cruz CS. Chitin and Its Effects on
931 Inflammatory and Immune Responses. Clinical Reviews in Allergy and
932 Immunology. Humana Press Inc.; 2018. pp. 213–223. doi:10.1007/s12016-
933 017-8600-0

64. Bashiri S, Koirala P, Toth I, Skwarczynski M. Carbohydrate immune adjuvants in subunit vaccines. Pharmaceutics. MDPI AG; 2020. pp. 1–33. doi:10.3390/pharmaceutics12100965
65. Bueter CL, Specht CA, Levitz SM. Innate Sensing of Chitin and Chitosan. PLoS Pathog. 2013;9. doi:10.1371/journal.ppat.1003080
66. Seetharaman J, Kfanigsberg A, Slaaby R, Leffler H, Barondes SH, Rini JM. X-ray crystal structure of the human galectin-3 carbohydrate recognition domain at 2.1-Å resolution. Journal of Biological Chemistry. 1998;273: 13047–13052. doi:10.1074/jbc.273.21.13047
67. Semeňuk T, Krist P, Pavlíček J, Bezouška K, Kuzma M, Novák P, et al. Synthesis of chitooligomer-based glycoconjugates and their binding to the rat natural killer cell activation receptor NKR-P1. Glycoconj J. 2001;18: 817–826. doi:10.1023/A:1021111703443
68. Zhou F, Wu S, Song S, Chen WR, Resasco DE, Xing D. Antitumor immunologically modified carbon nanotubes for photothermal therapy. Biomaterials. 2012;33: 3235–3242. doi:10.1016/j.biomaterials.2011.12.029
69. Nevagi RJ, Khalil ZG, Hussein WM, Powell J, Batzloff MR, Capon RJ, et al. Polyglutamic acid-trimethyl chitosan-based intranasal peptide nano-vaccine induces potent immune responses against group A streptococcus. Acta Biomater. 2018;80: 278–287. doi:10.1016/j.actbio.2018.09.037
70. Micoli F, Costantino P, Adamo R. Potential targets for next generation antimicrobial glycoconjugate vaccines. FEMS Microbiology Reviews. Oxford University Press; 2018. pp. 388–423. doi:10.1093/femsre/fuy011
71. National Institutes of Health. GUIDE LABORATORY ANIMALS FOR THE CARE AND USE OF Eighth Edition Committee for the Update of the Guide for the Care and Use of Laboratory Animals Institute for Laboratory Animal Research Division on Earth and Life Studies. 2011 [cited 6 Mar 2023]. Available: http://www.nap.edu.
72. Cisney ED, Fernandez S, Hall SI, Krietz GA, Ulrich RG. Examining the role of nasopharyngeal-associated lymphoreticular tissue (NALT) in mouse responses to vaccines. J Vis Exp. 2012 [cited 6 Mar 2023]. doi:10.3791/3960